The Astrophysical Journal, 816:53 (26pp), 2016 January 10 doi:10.3847/0004-637X/816/2/53

ERRATIC FLARING OF BL LAC IN 2012–2013: MULTIWAVELENGTH OBSERVATIONS

Ann E. Wehrle[1], Dirk Grupe[2,3], Svetlana G. Jorstad[4,5], Alan P. Marscher[4], Mark Gurwell[6], Mislav Baloković[7], Talvikki Hovatta[7,8], Grzegorz M. Madejski[9], Fiona H. Harrison[7], and Daniel Stern[10]
[1] Space Science Institute, 4750 Walnut Street, Suite 205, Boulder, CO 80301, USA; awehrle@spacescience.org
[2] Space Science Center, Morehead State University, 235 Martindale Drive, Morehead, KY 40351, USA
[3] Swift Mission Operation Center, 2582 Gateway Drive, State College, PA 16801, USA
[4] Institute for Astrophysical Research, Boston University, 725 Commonwealth Avenue, Boston, MA 02215, USA
[5] Astronomical Institute, St. Petersburg State University, Universitetskij Pr. 28, Petrodvorets, 198504 St. Petersburg, Russia
[6] Harvard-Smithsonian Center for Astrophysics, Cambridge, MA-02138, USA
[7] Cahill Center for Astronomy and Astrophysics, Caltech, Pasadena, CA 91125, USA
[8] Aalto University Metsähovi Radio Observatory, Metsähovintie 114, 02540 Kylmälä, Finland
[9] Kavli Institute for Particle Astrophysics and Cosmology, SLAC National Accelerator Laboratory, Menlo Park, CA 94025, USA
[10] Jet Propulsion Laboratory, California Institute of Technology, Pasadena, CA 91109, USA
Received 2015 February 26; accepted 2015 August 28; published 2016 January 5

ABSTRACT

BL Lac, the eponymous blazar, flared to historically high levels at millimeter, infrared, X-ray, and gamma-ray wavelengths in 2012. We present observations made with *Herschel, Swift, NuSTAR, Fermi*, the Submillimeter Array, CARMA, and the VLBA in 2012–2013, including three months with nearly daily sampling at several wavebands. We have also conducted an intensive campaign of 30 hr with every-orbit observations by *Swift* and *NuSTAR*, accompanied by *Herschel*, and *Fermi* observations. The source was highly variable at all bands. Time lags, correlations between bands, and the changing shapes of the spectral energy distributions can be explained by synchrotron radiation and inverse Compton emission from nonthermal seed photons originating from within the jet. The passage of four new superluminal very long baseline interferometry knots through the core and two stationary knots about 4 pc downstream accompanied the high flaring in 2012–2013. The seed photons for inverse Compton scattering may arise from the stationary knots and from a Mach disk near the core where relatively slow-moving plasma generates intense nonthermal radiation. The 95 spectral energy distributions obtained on consecutive days form the most densely sampled, broad wavelength coverage for any blazar. The observed spectral energy distributions and multi-waveband light curves are similar to simulated spectral energy distributions and light curves generated with a model in which turbulent plasma crosses a conical shock with a Mach disk.

Key words: BL Lacertae objects: individual (BL Lacertae) – galaxies: active – galaxies: individual (BL Lacertae) – galaxies: jets

Supporting material: machine-readable tables

1. INTRODUCTION

Blazars are the most highly variable class of active galactic nuclei (AGNs). Their emission is mainly nonthermal and originates in relativistic jets pointed within several degrees of our line of sight (see review by Urry & Padovani 1995). Doppler boosting enhances the amplitude and shortens the timescale of flux variations. BL Lac is the eponym and archetype of one of the two blazar classes, which include AGN with nearly featureless optical spectra (BL Lac objects) and flat spectrum radio quasars (FSRQs). The spectral energy distribution (SED) of a blazar contains two broad maxima, one at infrared (IR) to X-ray wavelengths with the characteristics of incoherent synchrotron radiation, and the other at γ-ray photon energies that is generally consistent with inverse Compton (IC) scattering. Some or all of the SED rises when the blazar flares, likely signalling a strong injection of energy in the form of charged particles into the relativistic jet, whose base is thought to lie several Schwarzschild radii from the central supermassive black hole. In all BL Lac objects and during flares in FSRQs, the nonthermal synchrotron and IC emission dominates over thermal emission from plasma accreting onto the black hole, hot dust, hot electrons in a "corona" near the black hole, and the stars in the host galaxy.

On 2012 April 9, the γ-ray emission from BL Lac rose to high flaring levels of $2.3\,(\pm0.03) \times 10^{-6}$ ph s^{-1} cm^{-2} (Cutini on behalf of The Fermi LAT Collaboration 2012), with a high optical R-band brightness of 13.1 mag measured the previous day (Larionov et al. 2012). It had already been experiencing a period of noticeable γ-ray and optical activity since spring 2011. In summer 2012, BL Lac underwent a major outburst at centimeter and millimeter wavelengths that soon extended into X-rays, reaching 30 year highs at all three bands (Ehgamberdiev et al. 2012; Grupe & Wehrle 2012; Karamanavis et al. 2012; Wehrle et al. 2012a). At γ-ray energies, the source began a several-month episode of highly variable brightness ranging chaotically from levels of 2.6×10^{-6} ph s^{-1} cm^{-2} down to non-detectable levels $<2.0 \times 10^{-7}$ ph s^{-1} cm^{-2} on timescales of 24 hr. The γ-ray light curve is illustrated in Figure 1; see also Figure 2 of Raiteri et al. (2013). Following reports of the flare, we obtained multiwavelength observations with the goals of determining answers to two questions: (1) In response to an injection of energy into the jet, is most of the multiwavelength emission from BL Lac produced in the same location or in multiple locations? (2) How are charged particles in BL Lac accelerated to nearly TeV-emitting energies? We attempt to answer these questions by modeling the SEDs during outbursts and

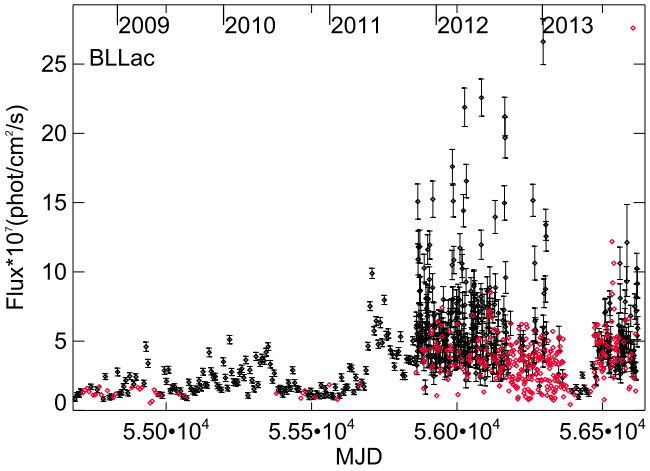

Figure 1. Light curve of BL Lac from 2008 August 8 to 2013 October 31, as observed with the *Fermi* LAT. Black filled diamonds indicate detections, red filled diamonds indicate upper limits. A mixture of integration times is used: 7-day integrations when the source was faint, and 1-day integrations when the source was bright.

measuring time delays between variations at millimeter, IR, optical, ultraviolet (UV), X-ray and γ-ray bands.

In BL Lac objects, the synchrotron peak in the SED lies in the IR, optical, UV, or X-ray bands, in contrast to FSRQs, in which the peak is always at IR wavelengths. The source of seed photons for IC scattering in BL Lac objects is thought to be synchrotron photons from the jet itself, unlike FSRQs where the external photon fields from the broad emission-line region and torus containing hot dust can play a major role. For some BL Lac objects and FSRQs, multiple sites of emission may be required to fit the observed multiwavelength SEDs (Nalewajko et al. 2012; Wehrle et al. 2012b, and references therein). BL Lac has broad H-α and H-β lines (Vermeulen et al. 1995) that vary in flux. Capetti et al. (2010) found that the broad H-α flux increased by 50% in ten years, which could indicate that the photoionizing radiation field from the accretion disk is variable or that there was an increase in the gas in the broad line region. In BL Lac, the broad line region may be underluminous compared to other AGN (Capetti et al. 2010). The discovery of even weak broad emission lines in BL Lac means that in some ways, BL Lac itself is more similar to FSRQs than to less luminous BL Lac objects such as Mkn 421 and Mkn 501 (see discussion in Madejski et al. 1999). Direct detection of an accretion disk in the UV–optical spectrum is rendered difficult by a substantial amount of Galactic dust absorption (see discussion in Raiteri et al. 2013). No parsec-scale dust internal to BL Lac objects that could serve as a source of seed photons for γ-ray production has yet been detected (Malmrose et al. 2011; Plotkin et al. 2012). Hence, if "external" photons are required as seed photons for IC scattering, they may come from pre-existing, localized, relatively slow-moving regions within the jet itself (e.g., in a sheath or Mach disk; MD), as distinguished from ambient synchrotron seed photons in the ultra-fast spine of the jet.

Several observational campaigns focusing on BL Lac have been carried out in the past few years. Abdo et al. (2011) completed a pre-planned multiwavelength campaign that caught BL Lac in a low, relatively quiescent state. Most recently, Raiteri et al. (2013) reported on *Fermi, Swift*, Submillimeter Array (SMA) and Whole Earth Blazar Telescope[11] observations beginning in 2008, through an episode of strong activity in 2011–2012, and continuing to 2012 October 31. Raiteri et al. also reviewed previous campaigns. Both their helical magnetic field model and square-wave shock model, each invoking a rapidly changing jet direction (ranging from an angle of 2°–6°.8 from the line of sight), reproduced fairly well the general pattern of the observed evolution of the polarization.

The present paper concentrates on observations beginning on 2012 October 27 and continuing for one year, with additional use of older data. The more recent period includes an extended interval of erratic changes in γ-ray flux, which sporadically reached the strongest levels yet observed in BL Lac, along with enhanced activity at other wavebands. Our data fill previous gaps in the SED through far-infrared (FIR) observations with *Herschel* and hard X-ray observations with *NuSTAR*, as well as dense coverage at UV and X-ray wavelengths with *Swift*. In this paper, we use $H_o = 70\,\mathrm{km\,s^{-1}\,Mpc^{-1}}$ and $\Omega_M = 0.28$ in a flat universe. We use three parameters corresponding to source brightness: flux density F_ν, measured in units of $\mathrm{W\,m^{-2}\,Hz^{-1}}$ (equivalently, Jy), energy flux F, in $\mathrm{W\,m^{-2}}$ (equivalently, $\mathrm{erg\,s^{-1}\,cm^{-2}}$), and photon flux S, in $\mathrm{ph\,cm^{-2}\,s^{-1}}$. When the spectrum is described as a power law, we define the slope of the flux density versus frequency dependence as the spectral index or energy index $-\alpha$, often with a subscript denoting the spectral band. The power-law slope of the photon flux dependence on frequency is defined as the photon index $-\Gamma = -(\alpha + 1)$.

2. OBSERVATIONS AND DATA ANALYSIS

2.1. Overview

The aims of our observing plan were to obtain light curves and SEDs with broad wavelength coverage. The observations featured FIR observations with the cryogenic *Herschel* mission[12] (Pilbratt et al. 2010). Our *Herschel* target of opportunity observations began on 2012 October 29 (MJD 56229) and continued for the three-month visibility window. We arranged for daily *Swift* pointings starting on 2012 October 27 through 2013 February 1, with a few gaps caused by moon avoidance and γ-ray burst observations. We also arranged for two intense periods of every-orbit *Swift* monitoring on 2012 December 11–12 and 2013 January11–12. The Large Area Telescope (LAT) instrument on *Fermi* operated in standard survey mode, scanning the entire sky every three hours. We obtained target of opportunity observations with *NuSTAR* on 2012 December 11–12. Observations of BL Lac every two to four days were carried out at the SMA on Mauna Kea, HI during the *Herschel* observation window, and intermittently thereafter. Monitoring observations with CARMA at 3 mm were already underway, and the cadence of observations was quickened during the months of the flares. VLBA monitoring continued throughout the time range reported here as part of the ongoing Boston University (BU) γ-ray blazar monitoring program. Observations at other wavebands were already underway by other collaborations, e.g., the Whole Earth Blazar Telescope. In addition, roughly weekly *Swift* observations have

[11] http://www.to.astro.it/blazars/webt/homepage.html

[12] *Herschel* is an ESA space observatory with science instruments provided by European-led Principal Investigator consortia and with important participation from NASA.

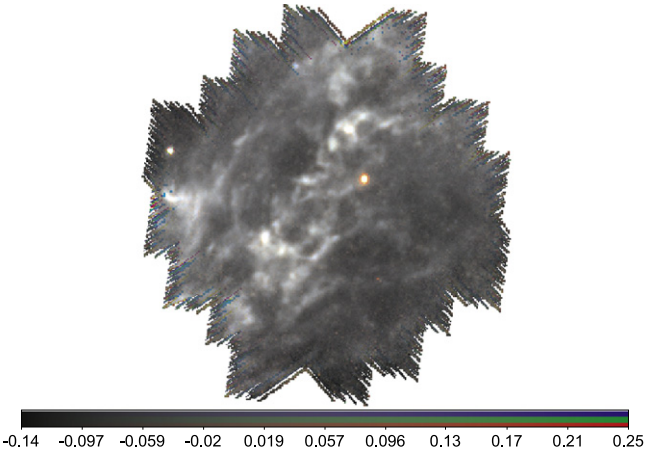

Figure 2. Wide-field *Herschel* SPIRE image of BL Lac and foreground Galactic nebular emission, obtained on 2012 May 13. BL Lac appears as the bright point source just to the right of image center. The field is approximately 37′ in diameter. Red: 500 μm, green: 350 μm, blue: 250 μm.

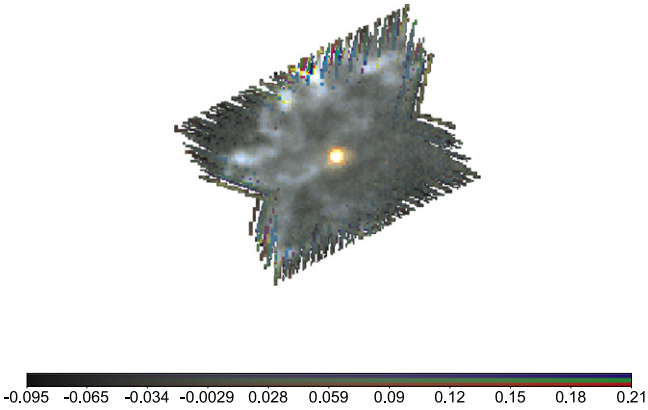

Figure 3. *Herschel* SPIRE image of BL Lac (bright source near center) and foreground Galactic nebular emission, obtained on 2013 January 21. The completely sampled center of the field is approximately 9′ in diameter. Red: 500 μm, green: 350 μm, blue: 250 μm.

been carried out for several years by A. Falcone and M. Stroh (Stroh & Falcone 2013).[13]

2.2. FIR Observations with the Herschel Space Observatory

Serendipitous *Herschel* SPIRE (Griffin et al. 2010) observations of BL Lac were made on 2012 May 13 at 500, 350 and 250 μm bands for the program led by M. Juvela to study cold cores in Galactic molecular clouds. Figure 2 shows the nebulous Galactic cloud emission in the foreground of the bright point source (at the resolution of *Herschel*) BL Lac; the field is approximately 37′ in diameter.

We carried out PACS-Photometer (Poglitsch et al. 2010) observations in "scan map" mode with 3-arcmin legs and a cross-scan step of 4 arcsec with a total on-source time of 72 s. Each PACS-Photometer observation included the "70 μm" (60–85 μm bandpass) and "160 μm" (130–210 μm bandpass) bands, consecutively with the "100 μm" (90–130 μm bandpass) and "160 μm" (130–210 μm bandpass) bands. The observations were carried out in consecutive pairs with different scan directions. The SPIRE-Photometer observations were done in "small map" mode with a total on-source time of 37 s, as in our previous observations of 3C454.3 (Wehrle et al. 2012b). We obtained a total of 38 PACS-Photometer images at each filter band (70, 160 μm) taken on 19 days between 2012 October 29 and 2013 January 29. Similarly, we obtained a total of 14 SPIRE-Photometer images at each filter band (250, 350, 500 μm) taken on 14 days between 2012 October 29 and 2013 January 21. On 8 days, we obtained both SPIRE and PACS data. For PACS, we derived flux densities from the *Herschel* pipeline images (version 9.0-9.2) from aperture photometry carried out in the *Herschel* Interactive Processing Environment (HIPE). Annular sky photometry using HIPE task "annularSkyAperturePhotometry" was used for PACS images, and aperture corrections applied as tabulated in Table 14 of the "PACS Photometer-Point Source Flux Calibration" document (version 1.0, 2011 April 12, *Herschel* Document PICC-ME-TN-037), Table 14. The PACS systematic error was 2.64% at 70 μm, 2.75% at 100 μm and 4.15% at 160 μm (PACS Photometer-Point Source Calibration, p. 23).

For the SPIRE measurements, we used Gaussian-fitting photometry on *Herschel* pipeline images (version 9.0-9.2), via HIPE task "sourceFitting," and then applied pixelization corrections as described in "The SPIRE Photometry Cookbook" (version 2011 May 3). SPIRE images of BL Lac show diffuse Galactic foreground emission and the bright point source of BL Lac (Figures 2 and 3). The background was smooth enough to use aperture fitting successfully with a small aperture. Timeline fitting gave similar results to within 1%. We use aperture fitting results in the Table. The SPIRE systematic error was 5% (SPIRE Photometry Cookbook, version 2011 May 3, and references therein).

The PACS intra-day measurement differences were less than 1%, well within the systematic errors; consequently, we averaged the measured flux densities for each day. We did not apply a color correction (equivalent to assuming that $F_\nu \propto \nu^{-\alpha}$, with $\alpha = 1$, or $\nu F_\nu =$ constant in SPIRE and PACS terminologies), since we did not know, a priori, the value of the spectral index over the *Herschel* bandpasses; we used the same approach in our 3C454.3 analysis (Wehrle et al. 2012b). We present the measured flux densities in Table 1, a composite 3-color SPIRE image of BL Lac and its surroundings on 2013 January 21 in Figure 3, and the light curves in Figure 4.

2.3. Millimeter and Submillimeter Band Observations with the SMA

BL Lac is occasionally used as an amplitude and phase calibrator at the SMA.[14] During the 2012 October to 2013 February period, we also observed the quasar as a science target. Data were reduced in the usual manner, as described in Gurwell et al. (2007) and Raiteri et al. (2013). Data obtained at 225 GHz (1.3 mm band) and 345 GHz (870 μm band) immediately before, during and after the *Herschel* observing period are listed in Table 1, with historical SMA data since 2002 in Tables 2 and 3. Uncertainties in the flux densities were dominated by systematic uncertainties of ∼5%. Data gaps occurred when the source transited the meridian in early- to mid-afternoon when the phase stability was often poor. Some of the data have been presented in graphical form in Raiteri

[13] http://www.swift.psu.edu/monitoring/

[14] http://sma1.sma.hawaii.edu/callist/callist.html/

Table 1
SMA and *Herschel* Data

Date	MJD	1.3 mm Flux Density (Jy)	1.3 mm Flux Density Error (Jy)	0.87 mm Flux Density (Jy)	0.87 mm Flux Density Error (Jy)	500 μm Flux Density[a] (Jy)	350 μm Flux Density[a] (Jy)	250 μm Flux Density[a] (Jy)	160 μm Flux Density[a,b] (Jy)	100 μm Flux Density[a,b] (Jy)	160 μm Flux Density[a,b] (Jy)	70 μm Flux Density[a,b] (Jy)
2012 Oct 29	56229	11.89	0.60	…	…	8.12	6.64	5.60	4.02	3.19	4.05	2.40
2012 Oct 29	56229	…	…	…	…	…	…	…	4.00	3.14	4.13	2.39
2012 Oct 30	56230	…	…	11.05	0.61	8.04	6.67	5.77	4.21	3.24	4.14	2.43
2012 Oct 30	56230	…	…	…	…	…	…	…	4.17	3.22	4.25	2.43
2012 Oct 31	56231	…	…	10.84	0.55	…	…	…	…	…	…	…
2012 Nov 1	56232	12.50	0.63	…	…	…	…	…	…	…	…	…
2012 Nov 2	56233	12.94	0.65	11.19	0.57	…	…	…	…	…	…	…
2012 Nov 3	56234	…	…	…	…	…	…	…	…	…	…	…
2012 Nov 4	56235	13.73	0.69	…	…	7.92	6.12	5.18	3.67	2.65	3.59	1.92
2012 Nov 4	56235	…	…	…	…	…	…	…	3.58	2.62	3.61	1.94
2012 Nov 5	56236	…	…	…	…	7.95	6.36	5.39	4.00	3.05	3.95	2.30
2012 Nov 5	56236	…	…	…	…	…	…	…	4.02	3.02	3.94	2.31
2012 Nov 6	56237	…	…	12.42	0.62	…	…	…	…	…	…	…
2012 Nov 7	56238	…	…	13.38	0.68	8.51	6.98	6.07	4.50	3.44	4.45	2.58
2012 Nov 7	56238	…	…	…	…	…	…	…	4.47	3.44	4.37	2.57
2012 Nov 8	56239	…	…	12.50	0.63	8.99	7.28	6.35	4.64	3.59	4.72	2.67
2012 Nov 8	56239	…	…	…	…	…	…	…	4.62	3.56	4.63	2.71
2012 Nov 9	56240	…	…	13.98	0.70	…	…	…	…	…	…	…
2012 Nov 10	56241	13.69	0.69	11.38	0.58	…	…	…	…	…	…	…
2012 Nov 11	56242	…	…	10.99	0.99	…	…	…	…	…	…	…
2012 Nov 12	56243	13.71	0.69	…	…	…	…	…	…	…	…	…
2012 Nov 13	56244	12.87	0.68	…	…	…	…	…	3.21	2.41	3.27	1.71
2012 Nov 13	56244	…	…	…	…	7.04	5.74	4.62	3.20	2.38	3.23	1.72
2012 Nov 14	56245	12.50	0.63	…	…	7.79	6.21	5.10	3.61	2.69	3.66	1.99
2012 Nov 14	56245	…	…	…	…	…	…	…	3.60	2.72	3.58	2.00
2012 Nov 15	56246	…	…	11.59	0.58	8.13	6.44	5.22	…	…	…	…
2012 Nov 16	56247	13.27	0.67	10.72	0.54	7.45	5.81	4.79	…	…	…	…
2012 Nov 17	56248	11.44	0.59	…	…	…	…	…	…	…	…	…
2012 Nov 18	56249	12.70	0.64	…	…	…	…	…	…	…	…	…
2012 Nov 19	56250	14.39	0.76	…	…	…	…	…	4.01	2.87	3.86	2.05
2012 Nov 19	56250	14.39	0.76	…	…	…	…	…	3.91	2.85	3.99	2.07
2012 Nov 20	56251	14.63	0.74	…	…	…	…	…	…	…	…	…
2012 Nov 21	56252	13.93	0.70	…	…	…	…	…	…	…	…	…
2012 Nov 22	56253	…	…	…	…	…	…	…	…	…	…	…
2012 Nov 23	56254	…	…	…	…	…	…	…	…	…	…	…
2012 Nov 24	56255	11.70	0.79	…	…	…	…	…	…	…	…	…
2012 Nov 25	56256	14.35	0.72	…	…	…	…	…	…	…	…	…
2012 Nov 26	56257	…	…	…	…	…	…	…	…	…	…	…
2012 Nov 27	56258	…	…	…	…	…	…	…	…	…	…	…
2012 Nov 28	56259	…	…	11.18	0.56	…	…	…	…	…	…	…
2012 Nov 29	56260	…	…	…	…	…	…	…	3.38	2.48	3.26	1.78
2012 Nov 29	56260	…	…	…	…	…	…	…	3.33	2.49	3.37	1.80
2012 Nov 30	56261	13.54	0.68	…	…	…	…	…	…	…	…	…
2012 Dec 1	56262	…	…	…	…	…	…	…	…	…	…	…
2012 Dec 2	56263	…	…	…	…	…	…	…	…	…	…	…
2012 Dec 3	56264	…	…	…	…	…	…	…	…	…	…	…
2012 Dec 4	56265	10.10	0.59	…	…	…	…	…	…	…	…	…
2012 Dec 5	56266	9.12	0.46	…	…	…	…	…	…	…	…	…
2012 Dec 6	56267	…	…	…	…	…	…	…	…	…	…	…
2012 Dec 7	56268	10.38	0.54	…	…	6.71	5.49	4.73	…	…	…	…
2012 Dec 8	56269	11.72	0.69	…	…	…	…	…	…	…	…	…
2012 Dec 9	56270	…	…	…	…	…	…	…	…	…	…	…
2012 Dec 10	56271	…	…	8.90	0.63	…	…	…	…	…	…	…
2012 Dec 11	56272	…	…	8.54	0.44	…	…	…	2.30	1.72	2.42	1.18
2012 Dec 11	56272	…	…	…	…	…	…	…	2.38	1.68	2.47	1.20
2012 Dec 12	56273	…	…	…	…	…	…	…	…	…	…	…
2012 Dec 13	56274	8.76	0.44	…	…	…	…	…	…	…	…	…
2012 Dec 14	56275	…	…	…	…	…	…	…	…	…	…	…
2012 Dec 15	56276	…	…	5.72	1.18	…	…	…	…	…	…	…
2012 Dec 16	56277	…	…	7.62	1.57	…	…	…	…	…	…	…

Table 1
(Continued)

Date	MJD	1.3 mm Flux Density (Jy)	1.3 mm Flux Density Error (Jy)	0.87 mm Flux Density (Jy)	0.87 mm Flux Density Error (Jy)	500 μm Flux Density[a] (Jy)	350 μm Flux Density[a] (Jy)	250 μm Flux Density[a] (Jy)	160 μm Flux Density[a,b] (Jy)	100 μm Flux Density[a,b] (Jy)	160 μm Flux Density[a,b] (Jy)	70 μm Flux Density[a,b] (Jy)
2012 Dec 17	56278	…	…	…	…	6.15	4.93	3.89	…	…	…	…
2012 Dec 18	56279	…	…	…	…	…	…	…	…	…	…	…
2012 Dec 19	56280	…	…	…	…	…	…	…	1.77	1.28	1.74	0.89
2012 Dec 19	56280	…	…	…	…	…	…	…	1.81	1.27	1.86	0.89
2012 Dec 20	56281	…	…	…	…	…	…	…	…	…	…	…
2012 Dec 21	56282	…	…	…	…	…	…	…	…	…	…	…
2012 Dec 22	56283	…	…	5.53	0.52	…	…	…	…	…	…	…
2012 Dec 23	56284	…	…	…	…	…	…	…	…	…	…	…
2012 Dec 24	56285	…	…	…	…	…	…	…	…	…	…	…
2012 Dec 25	56286	…	…	…	…	…	…	…	…	…	…	…
2012 Dec 26	56287	…	…	…	…	…	…	…	2.32	1.69	2.30	1.25
2012 Dec 26	56287	…	…	…	…	…	…	…	2.34	1.69	2.35	1.26
2012 Dec 27	56288	…	…	…	…	…	…	…	…	…	…	…
2012 Dec 28	56289	…	…	…	…	…	…	…	…	…	…	…
2012 Dec 29	56290	…	…	…	…	…	…	…	…	…	…	…
2012 Dec 30	56291	…	…	…	…	…	…	…	…	…	…	…
2012 Dec 31	56292	…	…	…	…	…	…	…	…	…	…	…
2013 Jan 1	56293	…	…	…	…	…	…	…	2.88	2.22	2.88	1.66
2013 Jan 1	56293	…	…	…	…	…	…	…	2.84	2.20	2.94	1.63
2013 Jan 2	56294	…	…	…	…	…	…	…	…	…	…	…
2013 Jan 3	56295	…	…	…	…	5.91	4.75	3.90	…	…	…	…
2013 Jan 4	56296	…	…	…	…	…	…	…	…	…	…	…
2013 Jan 5	56297	…	…	…	…	…	…	…	…	…	…	…
2013 Jan 6	56298	…	…	…	…	…	…	…	3.17	2.35	3.05	1.76
2013 Jan 6	56298	…	…	…	…	…	…	…	3.02	2.37	3.01	1.79
2013 Jan 7	56299	…	…	…	…	…	…	…	…	…	…	…
2013 Jan 8	56300	8.25	0.74	…	…	…	…	…	…	…	…	…
2013 Jan 9	56301	…	…	…	…	…	…	…	…	…	…	…
2013 Jan 10	56302	…	…	…	…	…	…	…	…	…	…	…
2013 Jan 11	56303	…	…	…	…	…	…	…	3.51	2.64	3.41	1.96
2013 Jan 11	56303	…	…	…	…	…	…	…	3.60	2.64	3.43	1.98
2013 Jan 12	56304	…	…	…	…	…	…	…	…	…	…	…
2013 Jan 13	56305	…	…	…	…	…	…	…	…	…	…	…
2013 Jan 14	56306	…	…	…	…	…	…	…	…	…	…	…
2013 Jan 15	56307	…	…	…	…	…	…	…	…	…	…	…
2013 Jan 16	56308	8.75	0.45	…	…	…	…	…	…	…	…	…
2013 Jan 17	56309	…	…	…	…	…	…	…	…	…	…	…
2013 Jan 18	56310	…	…	…	…	…	…	…	2.86	2.15	2.80	1.55
2013 Jan 18	56310	…	…	…	…	…	…	…	2.87	2.12	2.96	1.55
2013 Jan 19	56311	…	…	…	…	…	…	…	…	…	…	…
2013 Jan 20	56312	…	…	…	…	…	…	…	…	…	…	…
2013 Jan 21	56313	…	…	…	…	5.74	4.85	3.79	…	…	…	…
2013 Jan 22	56314	…	…	…	…	…	…	…	…	…	…	…
2013 Jan 23	56315	…	…	…	…	…	…	…	1.81	1.21	1.73	0.83
2013 Jan 23	56315	…	…	…	…	…	…	…	1.71	1.18	1.71	0.83
2013 Jan 24	56316	…	…	…	…	…	…	…	…	…	…	…
2013 Jan 25	56317	…	…	…	…	…	…	…	…	…	…	…
2013 Jan 26	56318	…	…	…	…	…	…	…	…	…	…	…
2013 Jan 27	56319	…	…	…	…	…	…	…	…	…	…	…
2013 Jan 28	56320	…	…	…	…	…	…	…	…	…	…	…
2013 Jan 29	56231	…	…	…	…	…	…	…	1.30	0.89	1.32	0.63
2013 Jan 29	56321	…	…	…	…	…	…	…	1.30	0.86	1.27	0.62

Notes.
[a] The errors are 5% at 500, 350 and 250 μm, 4.15% at 160 μm, 2.75% at 100 μm, and 2.64% at 70 μm.
[b] Data were taken at 160 and 100 μm simultaneously, followed a few minutes later by data taken at 160 and 70 μm simultaneously.

(This table is available in machine-readable form.)

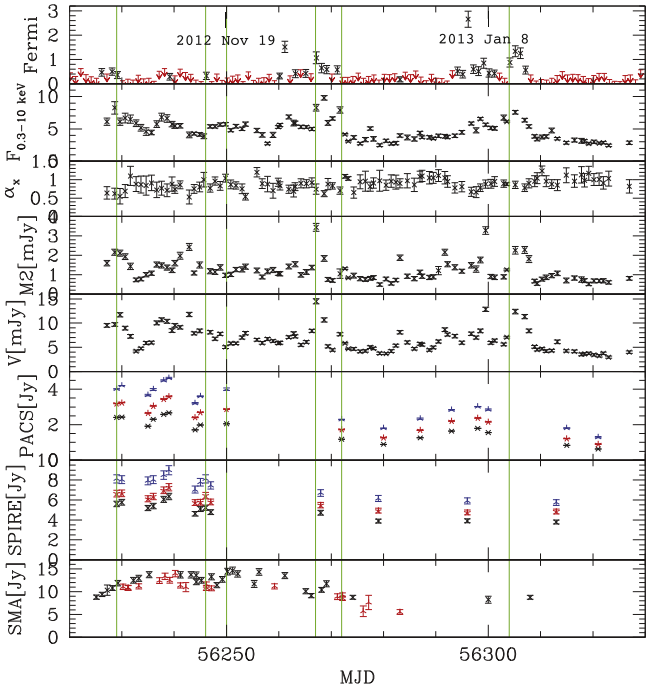

Figure 4. Light curves of BL Lacertae in 2012–2013. Top to bottom: *Fermi* LAT γ-ray curve in units of 10^{-6} ph cm^{-2} s^{-1}; *Swift* X-ray 0.3–10 keV energy flux in units of 10^{-11} erg s^{-1} cm^{-2}, uncorrected for Galactic absorption; *Swift* X-ray energy index α_X, calculated in XSPEC after correction for Galactic absorption was applied; *Swift* UVOT UVM2 band light curve in units of mJy, uncorrected for reddening or host galaxy contributions; *Swift* UVOT V-band light curve in units of mJy, uncorrected for reddening or host galaxy contributions; *Herschel* PACS (top to bottom) 160 (blue), 100 (red), 70 (black) μm fluxes in Jy; *Herschel* SPIRE (top to bottom) 500 (blue), 350 (red), 250 (black) μm fluxes in Jy; and SMA 225 GHz (black) and 345 GHz (red) light curves in Jy. Vertical lines are drawn at MJDs 56229, 56246, 56250, 56267, 56272, and 56304, for which SEDs are shown and modeled in this paper.

et al. (2013) and references therein. We present the light curves in Figures 5 and 6. We have measured both 225 and 345 GHz flux densities within an hour of each other on four days. The spectral indices varied from 0.81, 0.35, 0.42 and 0.45 $\pm$ 0.17 on 2012 October 12, 2012 November 2, 10, and 16 (MJDs 56212, 56233, 56241, and 56247), respectively. Systematic uncertainties of 5% were added in quadrature.

2.4. Millimeter Band Observations with CARMA

The CARMA data were obtained with the eight 3.5 m antennas as part of the Monitoring of γ-ray AGN with Radio, Millimeter and Optical Telescopes (MARMOT) project.[15] We used the full 7.5 GHz bandwidth with a center frequency of 94.75 GHz. The integration time on BL Lac was 5 minutes on each track, which yields a typical rms of 40–120 mJy. In all the observations a bright quasar was used as the passband calibrator, and BL Lac as the gain calibrator. Absolute flux density calibration was done using Mars, Neptune or Uranus, or a secondary calibrator 3C 345, which varies slowly. The observational errors are dominated by the absolute calibration uncertainty, assumed to be 10%. All data were processed using the Multichannel Image Reconstruction Image Analysis and Display (MIRIAD; Sault et al. 1995) software. The 94.75 GHz (3 mm) light curve is shown with the SMA 225 GHz (1.3 mm) light curve in Figure 7. The data from 2012 August 24 through 2013 October 29 (MJD 56163–56594) are given in Table 4.

[15] http://www.astro.caltech.edu/marmot/

2.5. Spectral Indices of FIR, Submillimeter and Millimeter Data

The far-IR spectral indices varied over the course of the observations, typically $\alpha_{IR} = 0.50$–0.97 in bands ranging from 500 to 70 μm. Data taken on the same days in the 225 GHz band with the SMA and at 94.75 GHz with CARMA yield spectral indices of 0.34, 0.30, and 0.4 $\pm$ 0.13 on 2012 November 10, 2012 November 20, and 2012 December 13, (MJDs 56241, 56251 and 56274), respectively. Note that the frequency of the SMA measurement was unusually low, 203.58 GHz, on 2012 December 13. These fairly flat spectral indices indicate that the flux was coming from multiple components rather than a single, uniform self-absorbed source, which would have a spectral index of $-5/2$. This type of flat spectrum is a common characteristic of compact radio sources. The 1.3 mm to 500 μm spectral indices were fairly flat: for example, on 29 October 2012 (MJD 56229), the spectral index was 0.39 $\pm$ 0.07. A series of SEDs covering mm-wave to far-IR bands demonstrates the variation from day to day (Figure 8). The rapid daily spectral index variations over the above range provide additional evidence for multiple emission regions with different physical characteristics within the jet.

2.6. Optical, UV, and X-Ray Observations with Swift

Table 5 presents the *Swift* observations of BL Lac during the monitoring period reported here between 2012 October 27 and 2013 October 31. We analyzed all available data obtained by the *Swift* UV/Optical Telescope (UVOT; Roming et al. 2005) during the monitoring period that produced measurements of the flux density of BL Lac in six filters, V (central wavelength: 5402 Å), B (4329 Å), U (3501 Å), UW1 (2634 Å), UM2 (2231 Å), and UW2 (2030 Å). We employed the UVOT software task *uvotsource* to extract counts within a circular region of 5 arcsec radius for the source and 20 arcsec radius for the background. The UVOT count rates were converted into magnitudes and fluxes based on the most recent UVOT calibration as described in Poole et al. (2008) and Breeveld et al. (2010). UVOT data in some of the tables (as indicated in the table footnotes) were corrected for Galactic reddening according to the corrections given in Raiteri et al. (2010), namely, 1.10, 1.44, 1.74, 2.40, 3.04, and 2.92 mag for the V, B, U, UW1, UM2, and UW2 bands, respectively.

The *Swift* X-ray telescope (XRT; Burrows et al. 2005) was operating in Photon Counting mode (Hill et al. 2004) for the observations between 2012 October 27 and 2012 November 8, and in Windowed Timing mode after 2012 November 9 in order to avoid the effects of pileup resulting from the high count rate of photons from BL Lac. The data were reduced by the task *xrtpipeline* version 0.12.6., which is included in the HEASOFT package 6.12. For the PC mode data the source counts were collected in a circle with a radius of 82.″5 excluding an inner radius of 11.″8. Background counts were selected in a source-free region with a radius of 247″ using the task *xselect* (version 2.4b). The WT source and background data were selected in a box with a length of 40 pixels. Auxillary response files were created using the XRT task *xrtmkarf*. The spectra were rebinned with 20 counts per bin using the task *grppha*. We applied the response files *swxpc0to12s6_*

Table 2
SMA 225 GHz Data

Date	UT	MJD	Frequency	Flux Density (Jy)	Flux Density Error (Jy)	PI
2002 Oct 11	0:00	52558.000	235.60	1.67	0.09	mgurwell
2002 Oct 29	0:00	52576.000	235.60	1.44	0.19	mgurwell
2003 Jan 18	6:33	52657.273	235.60	1.31	0.20	mgurwell
2003 Apr 18	4:41	52747.195	238.00	2.26	0.39	mgurwell
2003 Jun 3	5:23	52793.223	229.00	2.68	0.30	mgurwell

(This table is available in its entirety in machine-readable form.)

Table 3
SMA 345 GHz Data

Date	UT	MJD	Frequency	Flux Density (Jy)	Flux Density Error (Jy)	PI
2002 Jun 6	0:00	52431.000	340.70	1.40	0.43	mgurwell
2002 Nov 23	0:00	52601.000	340.70	1.91	0.19	mgurwell
2002 Nov 24	0:00	52602.000	340.70	2.32	0.23	mgurwell
2004 Jul 27	11:30	53213.480	305.78	2.03	0.18	mgurwell
2004 Jul 28	6:36	53214.273	340.78	2.13	0.29	mgurwell
2004 Aug 12	4:10	53229.172	340.75	1.60	0.18	mgurwell

(This table is available in its entirety in machine-readable form.)

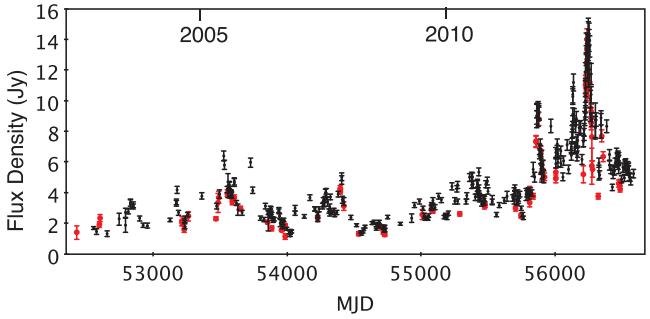

Figure 5. SMA light curves of BL Lacertae in 2002–2013. Data at 225 GHz (1.3 mm) and 345 GHz (870 μm) are shown in black and red circles, respectively. Data sources include the SMA Calibrator Program of M. Gurwell, a 2008–2010 monitoring program led by A. Wehrle, and new Target of Opportunity observations obtained for the program reported here.

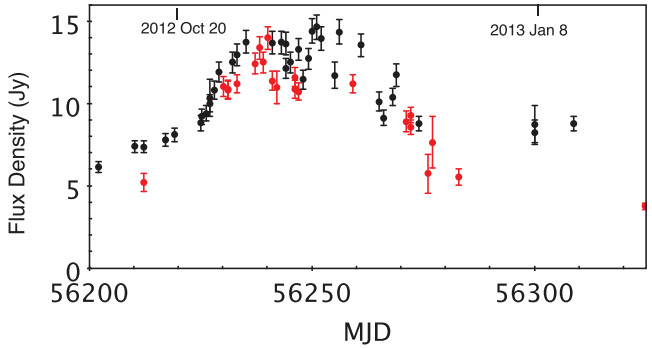

Figure 6. SMA light curves of BL Lacertae during the peak of the millimeter-wave flaring in 2012 December 30 to 2013 February 2 (MJD 56200–56325). Data at 225 GHz (1.3 mm) and 345 GHz (870 μm) are displayed in black and red circles, respectively. Occasional data gaps occurred when the source transited the meridian in early- to mid-afternoon when the phase stability was often poor.

20010101v013.rmf and *swxwt0to2s6_20070901v012.rmf* to the pc and WT data, respectively. The rebinned spectra were modeled within 0.3–10 keV in XSPEC v.12.7 with a single power-law continuum and Galactic absorption corresponding to a hydrogen column density $N_{\rm H} = 3.4 \times 10^{21}$ cm^{-2} (Raiteri et al. 2010). The derived 0.3–10 keV fluxes and X-ray energy indices $\alpha_{\rm X}$ are listed in Table 6. Light curves are shown in Figures 4 and 9. Host galaxy contributions were subtracted, where appropriate, in the resulting SEDs using the values calculated by Raiteri et al. (2013): 50% of the host galaxy flux was contained within the 5″ aperture. Consequently, we subtracted 0.5 × (2.89, 1.30, 0.36, 0.026, 0.020, 0.017) mJy for the V, B, U, UW1, UM2, and UW2 bands, respectively. Host-galaxy-subtracted and de-reddened values are used in some tables and figures where appropriate.

2.6.1. UV and Optical Spectral Indices

The optically thin synchrotron emission has steep spectral indices; for example, $\alpha_{\rm UV} = 1.68 \pm 0.08$ (after dereddening and removal of the host galaxy contribution) between the V and UVW2 bands on the date of highest flux, 2012 October 29 (MJD 56229). In general, the spectra are steeper when the source is bright, and flatter when it is faint. If we attribute the

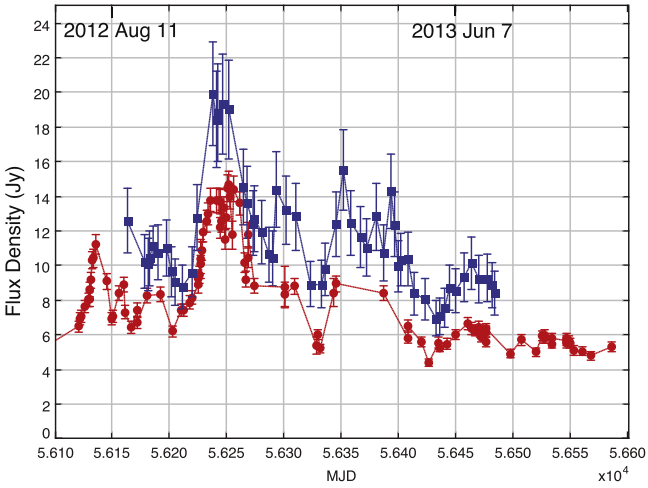

Figure 7. Light curves of BL Lacertae at 94.75 GHz (3 mm; blue squares) with CARMA and at 225 GHz (1.3 mm; red filled circles) with the SMA for comparison.

increase in flux to a single, rapidly variable component as a thought experiment, we can obtain its spectrum by subtracting the total spectrum on the lowest day (MJD 56280) from that on the highest day (MJD 56229). The resulting spectrum has $\alpha = 1.8 \pm 0.1$, but with a flat spectral index between UVM2 and UVW2 bands. The latter is consistent with flattening of the electron energy distribution at high energies. However, we note that the spectral index between UVM2 and UVW2 is highly uncertain due to both calibration problems and difficulties in determining the extinction in the UV. We also plot the spectral index in the UV and X-ray bands as a function of time in Figure 10. A mild anti-correlation is apparent to the eye; as noted earlier, the Spearman rank correlation coefficient is -0.34 for 173 data points, which corresponds to a probability of only 3.8×10^{-6} that there is no anti-correlation. The anti-correlation is most readily understood if the soft X-ray flux contains a contribution from both a steep-spectrum synchrotron and a flatter-spectrum IC component, as indicated by the difference between the spectral indices measured at the same time by *Swift* and *NuSTAR* (see below). The same synchrotron component is presumed to dominate the UV flux, but with a flatter spectrum than at X-ray energies. If the UV spectrum becomes flatter with time, corresponding to a shift of the synchrotron SED to higher frequencies, the soft X-ray flux will rise as the flux of its synchrotron component increases. Since the X-ray synchrotron emission has a steeper slope than the IC component, the soft X-ray spectrum will steepen, thus causing the observed anti-correlation.

2.6.2. Low Energy X-Ray Spectrum

We group the *Swift* XRT data in low, medium and high states in order to determine whether the energy index changed when the source was brighter or fainter. We define the low state as (2–4) $\times 10^{-11}$, medium state as (4–6) $\times 10^{-11}$, and high state as $>6 \times 10^{-11}$ erg s^{-1} cm^{-2}. As seen in Figure 11, brighter states tend to have harder X-ray spectra: for low, medium and high states $\alpha_X = 0.97 \pm 0.01$, 0.86 ± 0.01, and 0.67 ± 0.03, respectively. This is readily apparent in historical data at 2–10 keV from the *Rossi X-ray Timing Explorer* (*RXTE*) displayed in appendix. We note, however, that flat X-ray

Table 4
CARMA Data

Date	UT	MJD	94.75 GHz Flux Density (Jy)	94.75 GHz Flux Density Error (Jy)
2012 Aug 24	6:01	56163.25	12.65	1.27
2012 Sep 08	4:57	56178.21	9.84	0.98
2012 Sep 11	5:14	56181.22	9.48	0.95
2012 Sep 12	5:12	56182.22	9.76	0.98
2012 Sep 15	3:30	56185.15	10.65	1.06
2012 Sep 20	4:11	56190.17	9.15	0.92
2012 Sep 27	7:19	56197.31	10.06	1.01
2012 Oct 01	2:45	56201.12	8.72	0.87
2012 Oct 04	6:25	56204.27	8.14	0.81
2012 Oct 11	1:53	56211.08	8.74	0.87
2012 Oct 19	5:34	56219.23	8.73	0.87
2012 Oct 24	4:32	56224.19	12.05	1.20
2012 Nov 07	1:04	56238.04	18.02	1.80
2012 Nov 10	4:24	56241.18	16.90	1.69
2012 Nov 10	23:20	56241.97	15.11	1.51
2012 Nov 14	23:04	56245.96	17.12	1.71
2012 Nov 20	22:43	56251.95	15.71	1.57
2012 Dec 03	3:20	56264.14	13.14	1.31
2012 Dec 06	1:53	56267.08	12.55	1.25
2012 Dec 11	20:40	56272.86	11.40	1.14
2012 Dec 13	1:49	56274.08	11.56	1.16
2012 Dec 25	20:28	56286.85	10.00	1.00
2012 Dec 28	20:02	56289.84	11.43	1.14
2013 Jan 01	0:27	56293.02	13.10	1.31
2013 Jan 09	19:30	56301.81	12.30	1.23
2013 Jan 17	19:32	56309.81	11.69	1.17
2013 Jan 30	18:19	56322.76	7.92	0.79
2013 Feb 08	22:01	56331.92	8.28	0.83
2013 Feb 12	21:42	56335.90	8.76	0.88
2013 Feb 21	17:52	56344.74	10.59	1.06
2013 Feb 28	20:56	56351.87	14.63	1.46
2013 Mar 06	17:06	56357.71	11.07	1.11
2013 Mar 15	16:08	56366.67	10.56	1.06
2013 Mar 20	21:52	56371.91	11.00	1.10
2013 Mar 29	13:33	56380.56	12.06	1.21
2013 Apr 04	16:00	56386.67	9.74	0.97
2013 Apr 10	13:46	56392.57	11.73	1.17
2013 Apr 14	15:08	56396.63	10.41	1.04
2013 Apr 17	16:59	56399.71	9.01	0.90
2013 Apr 19	14:16	56401.59	9.39	0.94
2013 Apr 25	12:49	56407.53	8.99	0.90
2013 May 01	17:35	56413.73	7.63	0.76
2013 May 10	12:32	56422.52	7.26	0.73
2013 May 20	11:11	56432.47	6.32	0.63
2013 May 23	11:29	56435.48	6.35	0.64
2013 May 27	10:39	56439.44	7.49	0.75
2013 Jun 01	10:20	56444.43	8.01	0.80
2013 Jun 06	10:59	56449.46	7.76	0.78
2013 Jun 13	13:21	56456.56	8.46	0.85
2013 Jun 20	8:26	56463.35	9.02	0.90
2013 Jun 26	14:26	56469.60	8.42	0.84
2013 Jul 04	7:50	56477.33	8.13	0.81
2013 Jul 08	6:49	56481.28	7.79	0.78
2013 Jul 10	6:41	56483.28	7.39	0.74
2013 Jul 18	7:00	56491.29	6.97	0.70
2013 Jul 19	6:39	56492.28	6.74	0.67
2013 Jul 24	10:54	56497.45	6.26	0.63
2013 Aug 05	10:18	56509.43	6.57	0.66
2013 Aug 12	9:57	56516.42	6.51	0.65
2013 Aug 19	4:37	56523.19	7.05	0.71

Table 4
(Continued)

Date	UT	MJD	94.75 GHz Flux Density (Jy)	94.75 GHz Flux Density Error (Jy)
2013 Aug 24	4:56	56528.21	7.20	0.72
2013 Aug 29	5:55	56533.25	7.23	0.72
2013 Sep 08	3:09	56543.13	7.21	0.72
2013 Sep 22	2:39	56557.11	5.92	0.59
2013 Oct 01	1:43	56566.07	6.09	0.61
2013 Oct 06	6:09	56571.26	5.48	0.55
2013 Oct 13	3:25	56578.14	5.62	0.56
2013 Oct 16	3:05	56581.13	5.41	0.54
2013 Oct 20	0:28	56585.02	5.19	0.52
2013 Oct 25	2:16	56590.09	5.16	0.52
2013 Oct 29	1:39	56594.07	5.22	0.52

(This table is available in machine-readable form.)

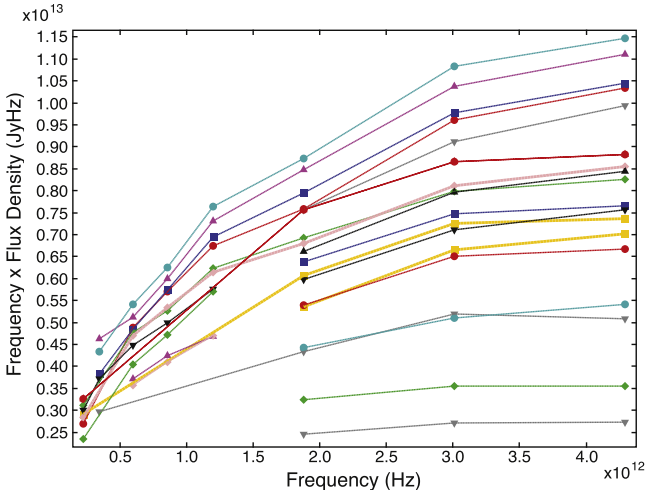

Figure 8. Millimeter to infrared SEDs from 2012 October to 2013 February, showing a variety of shapes from one day to another. Error bars, ranging from 5% to 2.64%, are too small to be shown.

spectra sometimes occur at low flux levels. Over the *RXTE* energy range, the emission appears to be dominated by the flatter-spectrum IC component at high flux levels, while in lower states the steep-spectrum synchrotron component is often significant.

2.7. Hard X-Ray Observations with NuSTAR

NuSTAR, launched on 2012 June 13, is a hard X-ray satellite, carrying the first telescope in orbit capable of focusing in the relatively under-explored 3–79 keV band (Harrison et al. 2013). The telescope consists of two co-aligned optical systems in front of two focal plane modules (FPMA and FPMB) covered by 2 × 2 arrays of CdZnTe pixel detectors surrounded by CsI anti-coincidence shields. The resulting low background enables *NuSTAR* to achieve approximately a hundred-fold improvement in sensitivity over the collimated or coded-mask instruments that operate, or have operated, in the same bandpass.

BL Lac was observed with *NuSTAR* on 2012 December 11 and 12 (ObsID 60001001002). The observation extended over 8 *NuSTAR* orbits, totaling 22.1 ks of exposure, as detailed in Table 7. The data were processed using the *NuSTAR* Data Analysis Software (NuSTARDAS) version 1.4.1 with calibration files from CALDB version 20131223. Spectra for the whole observation and each orbit separately were extracted from a circular region 60″ in radius, centered on the source. Background was extracted from a source-free region on the same detector on which the target was focused, which best approximates the background underlying the target. The target is detected above the background up to ≃65 keV. The response files were produced by the pipeline task `numkarf`, and include PSF correction for a finite extraction region, the exposure map, and bad pixels. Absolute calibration agrees to within 15% with other X-ray observatories across the 3–10 keV band based on dedicated cross-calibration observations (Madsen et al., *submitted*). Joint fitting for *NuSTAR* FPMA and FPMB spectra was performed in XSPEC version 12.8.2. The spectra were grouped into a minimum of 50 photons per bin using the `grppha` task. All uncertainties are reported as 1σ (68% confidence level). We fix the hydrogen column density to $N_{\rm H} = 3.4 \times 10^{21}$ cm^{-2}, including both the Galactic absorption and the absorption by the Galactic molecular cloud noted earlier. A statistically good fit to the whole *NuSTAR* observation is a simple power-law model with a photon index $\Gamma = 1.88 \pm 0.01$ (recall $\Gamma = \alpha_{\rm X} + 1$). This fit has a $\chi^2 = 287$ for 283 degrees of freedom. Modeling the *NuSTAR* spectrum as a broken power law or log-parabola does not significantly improve the fit further, but we list the best-fit parameters in Table 8 for completeness. As there is no obvious spectral break within the *NuSTAR* bandpass, the break energy of the broken power law model is completely unconstrained, so we fix it (arbitrarily) at 7 keV. We use the same energy as a pivot for the log-parabolic model, so that the α parameter corresponds to the photon index at that energy.

The *NuSTAR* observation overlaps in time with two *Swift* observations of BL Lac (segments 050 and 053; 2.6 and 1.7 ks of contemporaneous exposure, respectively). Time intervals overlapping with the *NuSTAR* observation were selected and processed as described in Section 2.6. The contemporaneous *NuSTAR* and *Swift*/XRT data, covering the broadband spectrum between 0.5 and 65 keV, are simultaneously fit in XSPEC with the cross-normalization constants allowed to vary freely. Assuming a power-law model with fixed $N_{\rm H}$, we find $\Gamma = 1.89 \pm 0.01$ ($\chi^2 = 385$ for 375 degrees of freedom). The broken power-law and log-parabolic models improve the fit marginally; χ^2 decreases by 4 per degree of freedom for two additional parameters in the former and one in the latter model. The residuals of all three models are shown in Figure 12, and their parameters are listed in Table 8. Results of the joint fitting indicate that the observed X-ray spectrum may be "concave," i.e., steeper at softer than at harder photon energies. In order to account for an apparent excess at the low-energy end of the *Swift*/XRT band with respect to a simple power law (see Figure 12), the broken power-law model includes a steep $\Gamma \gtrsim 3$ slope below 1 keV, however, this is poorly constrained with the contemporaneous *Swift*/XRT data. The log-parabolic model fit suggests a marginally negative curvature parameter, $\beta_{Xlp} = -0.04 \pm 0.03$, but does not fully account for the low-energy excess.

Table 5
Swift Observation log of BL Lac (ObsID 30720 and 35028)

Target ID	Segment	T-start[a]	T-stop[a]	MJD[b]	T_{XRT}[c]	T_V[c]	T_B[c]	T_U[c]	T_{UVW1}[c]	T_{UVM2}[c]	T_{UVW2}[c]
30720	005	2012 Oct 27 03:56	2012 Oct 27 04:13	56227.169714	994	82	82	82	164	238	328
	006	2012 Oct 28 15:12	2012 Oct 28 15:29	56228.639207	989	80	80	80	159	250	319
	007	2012 Oct 29 15:15	2012 Oct 29 15:32	56229.641324	1001	80	80	80	160	250	320
	008	2012 Oct 30 15:18	2012 Oct 30 15:35	56230.643465	991	79	79	79	157	252	315
	009	2012 Oct 31 15:21	2012 Oct 31 15:32	56231.643365	647	51	51	51	102	162	205
	010	2012 Nov 01 17:16	2012 Nov 01 17:33	56232.725319	996	80	80	80	159	255	319
	011	2012 Nov 02 15:28	2012 Nov 02 15:44	56233.649925	942	75	75	75	150	243	300
	012	2012 Nov 03 15:30	2012 Nov 03 15:46	56234.651314	942	75	75	75	150	244	300
	013	2012 Nov 04 15:32	2012 Nov 04 15:50	56235.653378	1007	85	85	85	171	269	343
	014	2012 Nov 05 15:35	2012 Nov 05 15:52	56236.655190	1001	80	80	80	159	254	319

Notes.
[a] Start and end times are given in UT.
[b] MJD listed marks the middle of the observation.
[c] Observing time given in seconds.
(This table is available in its entirety in machine-readable form.)

The concave spectral shape is further supported by the energy index $\alpha_X = 1.09 \pm 0.05$ (equivalently, $\Gamma = 2.09 \pm 0.05$) found from the non-contemporaneous 7.9-ks *Swift*/XRT exposure immediately preceeding the *NuSTAR* observation. Note that this is consistent with some previous results in the literature, e.g., Tanihata et al. (2000). A plausible explanation is that the high-frequency end of the synchrotron spectrum is often significant at energies below several keV, while IC emission dominates at harder energies. If the former is true, we would expect the soft X-ray spectrum to contain a greater contribution from the synchrotron component—and therefore a higher energy index—when the UV spectrum is flatter. Figure 10 plots the *Swift* 0.3–10 keV X-ray and UV spectral indices as a function of time. The expected trend is apparent in this curve, and a modest anti-correlation is seen in the inset α_X versus α_{UV} scatter plot. See Section 2.6.1 for further discussion of this relationship.

High photon statistics allow the *NuSTAR* data to be separated into particular 2.5–3.5 ks orbits with sufficient number of counts to perform spectral fits up to approximately 50 keV. Fluxes in energy bands of 3–7, 7–15, 15–31 and 31–63 keV and best-fit photon indices derived from a joint power-law model fit to both *NuSTAR* FPMs are listed in Table 7. Figure 13 shows the *NuSTAR* light curve in physical flux units and the variation of the fitted photon indices. Mild variability on timescales of single *NuSTAR* orbits ($\sim$1.5 hr) is apparent, with flux changes of up to 30% relative to the mean, or a factor of a few above the 1σ flux uncertainty level.

2.8. γ-ray Observations with Fermi Gamma-ray Space Telescope

We downloaded Pass 7 photon and spacecraft data from the *Fermi* Science Support Center for an area with radius 15° centered on BL Lacertae at energies from 0.1 to 200 GeV from 2008 August 5 (MJD 54683) to 2013 October 31 (MJD 56596). We used version V9r31p5 of the *Fermi* Science Tools and the instrument responses gll_iem_v05.fit and iso_source_v05.txt for the diffuse source models. We fixed the spectral parameters of sources within the area according to the 2FGL catalog (Nolan et al. 2012) and searched for the values of flux normalization parameters by applying the standard unbinned likelihood analysis. We have constructed several γ-ray light curves for BL Lacertae:

1. *Light curve 1: one-week integrations with a fixed log-parabolic spectrum.* For light curves 1–3, the spectral model of BL Lacertae was fixed to that given in the 2FGL catalog—a log-parabolic shape of the photon flux spectrum as a function of the energy E_γ:

$$S(E_\gamma) = S_0 (E_\gamma/E_b)^{-(\alpha_\gamma + \beta_\gamma \ln(E_\gamma/E_b))}, \quad (1)$$

with $\alpha_\gamma = 2.1069$, $\beta_\gamma = 0.0950$, and $E_b = 388.49$ MeV. For light curve 1, the photon data were integrated within bin sizes of one week. The flux was considered detected if the test statistic, TS, provided by the analysis exceeded 10, which corresponds to approximately a 3σ detection level (Nolan et al. 2012). This criterion was used for all γ-ray light curves to discriminate between detections and non-detections. This criterion produced 225 detections out of 273 measurements. The γ-ray flux reached a maximum of $(1.066 \pm 0.083) \times 10^{-6}$ ph cm^{-2}s^{-1} on 2012 August 24 (MJD 56163).
2. *Light curve 2: one-day integrations with a fixed log-parabolic spectrum.* Based on visual inspection of light curve 1, we have selected the period from 2011 February 8 (MJD 55600) to 2013 October 31 as the time span of highest γ-ray activity. With a bin size of one day, the light curve consists of 1005 measurements with 502 detections. The maximum flux of $(2.66 \pm 0.33) \times 10^{-6}$ ph cm^{-2} s^{-1} occurred on 2013 January 4 (MJD 56296).
3. *Light curve 3: 6-hr integrations with a fixed log-parabolic spectrum.* Analysis of light curve 2 showed that the majority of 24-hr detections were obtained between 2011 March 18 and 2013 May 11 (MJD 55700–56371). Over this period, we have computed quarter-day fluxes with a bin size of 6 hr. The light curve consists of 2918 measurements with 609 detections. The maximum γ-ray flux, $(5.025 \pm 0.908) \times 10^{-6}$ ph cm^{-2} s^{-1}, was observed on 2013 January 4 (MJD 56296.03).

Table 6
Observed 0.3–10 keV Fluxes, X-Ray Energy Indices α_X, and UVOT Flux Densities of BL Lac

Target ID	Segment	MJD	$F_{0.3-10\ keV}$[a]	α_X[a]	f_V[b]	f_B[b]	f_U[b]	f_{W1}[b]	f_{M2}[b]	f_{W2}[b]
30720	005	56227.1697	4.55 ± 0.42	0.64 ± 0.17	9.54 ± 0.38	6.08 ± 0.22	3.92 ± 0.16	2.30 ± 0.13	1.59 ± 0.14	1.49 ± 0.09
	006	56228.6392	6.21 ± 0.74	0.62 ± 0.15	9.73 ± 0.39	6.80 ± 0.24	3.91 ± 0.17	2.34 ± 0.13	2.16 ± 0.16	1.49 ± 0.09
	007	56229.6413	5.00 ± 0.46	0.55 ± 0.21	11.73 ± 0.44	7.32 ± 0.25	4.79 ± 0.19	2.72 ± 0.14	2.11 ± 0.16	1.87 ± 0.10
	008	56230.6435	5.28 ± 0.60	0.69 ± 0.18	8.98 ± 0.37	6.28 ± 0.23	4.01 ± 0.17	2.25 ± 0.13	1.93 ± 0.15	1.57 ± 0.09
	009	56231.6434	4.48 ± 0.44	1.10 ± 0.26	7.26 ± 0.39	4.68 ± 0.23	3.01 ± 0.17	1.43 ± 0.13	1.43 ± 0.16	0.94 ± 0.09
	010	56232.7253	4.41 ± 0.38	0.88 ± 0.20	4.22 ± 0.24	2.91 ± 0.15	1.52 ± 0.10	0.95 ± 0.08	0.73 ± 0.10	0.54 ± 0.06
	011	56233.6499	3.85 ± 0.39	0.87 ± 0.23	4.76 ± 0.27	3.28 ± 0.16	1.90 ± 0.11	1.03 ± 0.09	0.78 ± 0.10	0.71 ± 0.06
	012	56234.6513	3.44 ± 0.44	0.84 ± 0.26	5.88 ± 0.30	3.90 ± 0.17	2.12 ± 0.12	1.18 ± 0.10	1.00 ± 0.11	0.77 ± 0.07
	013	56235.6534	3.32 ± 0.28	0.91 ± 0.21	5.96 ± 0.28	4.16 ± 0.17	2.24 ± 0.12	1.39 ± 0.10	1.07 ± 0.11	0.98 ± 0.07
	014	56236.6552	4.48 ± 0.40	0.72 ± 0.21	10.04 ± 0.40	6.82 ± 0.24	4.27 ± 0.18	2.18 ± 0.13	1.52 ± 0.13	1.23 ± 0.08

Notes.
[a] Observed 0.3–10 keV flux in units of 10^{-11} erg s^{-1} cm^{-2} (10^{-14} W m^{-2}), uncorrected for Galactic absorption. Values of α_X were calculated in XSPEC after correction for Galactic absorption was applied.
[b] Reddening-corrected flux densities in units of mJy (10^{-29} W m^{-2} Hz^{-1}). Reddening correction was performed according to the correction factors given in the text, as taken from Raiteri et al. (2013).
[c] No reliable flux can be given because the source was at the edge of the WT window.

(This table is available in its entirety in machine-readable form.)

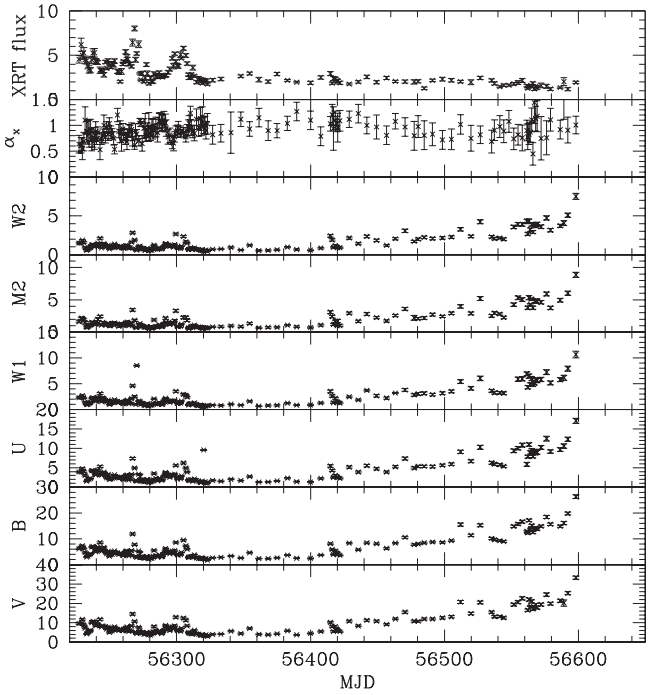

Figure 9. Light curves of BL Lacertae from 2012 October 27 to 2013 October 31. Top to bottom: *Swift* X-ray 0.3–10 keV energy flux in units of 10^{-11} erg s^{-1} cm^{-2}, uncorrected for Galactic absorption; *Swift* X-ray energy index α_X, calculated in XSPEC after correction for Galactic absorption was applied. *Swift* UVOT UVW2, UVM2, UVW1, U, B, and V band light curve in units of mJy after dereddening and correction for host galaxy contributions.

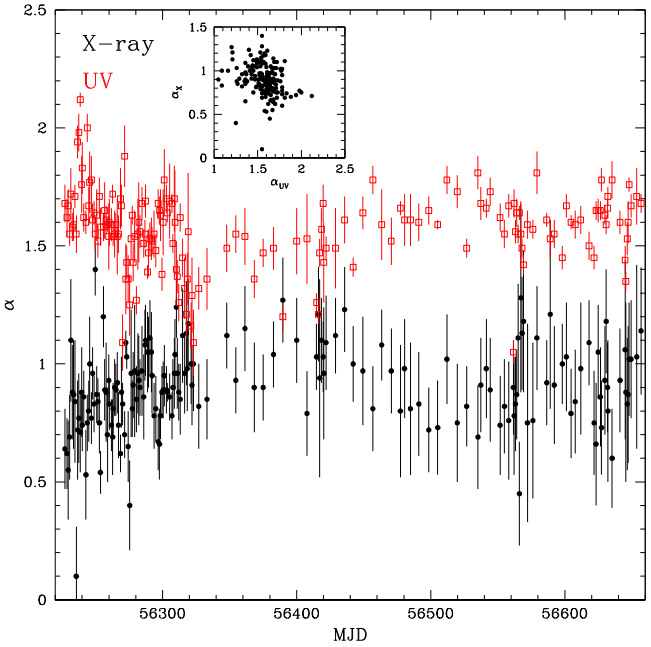

Figure 10. UV spectral index and *Swift* 0.3–10 keV X-ray energy index vs. time for BL Lac. The inset presents a scatter plot of the two indices. A modest anti-correlation is apparent, as expected if the synchrotron emission component that dominates at UV wavelengths contributes a significant fraction of the soft X-ray flux.

4. *Light curve 4: one-week integrations with a variable power-law spectrum.* Over the same time span as light curve 2, we have calculated fluxes for a simple power-law model with variable photon index $\Gamma_\gamma^{\rm var}$. The light curve consists of 143 measurements with 126 detections. The maximum flux is the same (within 1σ uncertainty) as for light curve 1, $(1.047 \pm 0.091) \times 10^{-6}$ ph cm^{-2} s^{-1}. Although the photon index varies between 2.0 and 3.1, the average value of $\Gamma_\gamma^{\rm var} = 2.32$ has a standard deviation of 0.23, which is only slightly larger than the average 1σ uncertainty of individual measurements, 0.17.

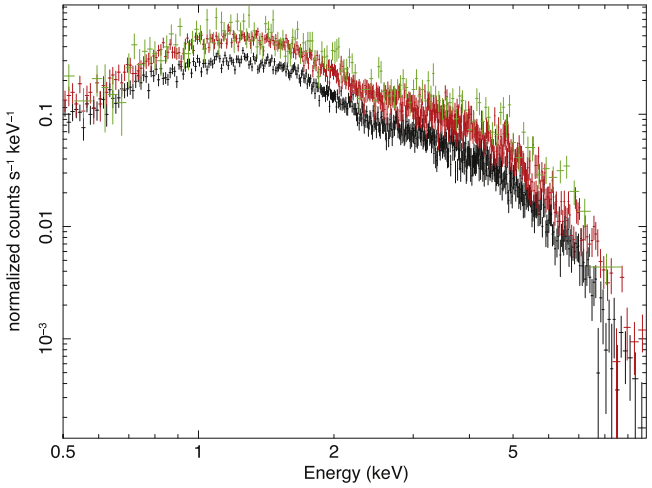

Figure 11. X-ray spectra of BL Lac at high (green), medium (red), and low (black) states. The spectrum tends to be harder during brighter states.

Figure 14 shows light curves (from the top) 4, 2, and 3 (only detections for light curve 3) and dependence of $\Gamma_\gamma^{\rm var}$ on time. There is a slight hardening of the spectrum (within 1σ uncertainty) in the beginning of the γ-ray activity state, MJD 55700–55800. Note also the increase of the γ-ray maximum flux for shorter time bins.

2.8.1. γ-ray Spectrum

We have calculated the γ-ray 0.1–200 GeV power-law photon index on the days on which BL Lac was detected by the *Fermi* LAT. The mean value from 2009 November to 2013 October is $\Gamma_\gamma = 2.28 \pm 0.19$, with a maximum of 3.12 and minimum of 1.98. Inspection of Figures 15 and 16 reveals that the steepest spectra occurred only when the flux was below 0.5×10^{-6} ph cm^{-2} s^{-1}, while values within 1σ of the mean occurred over the full flux range. We also fit a log parabolic model to the 7-day integrations; however, most of the detections were not strong enough to allow the log parabolic model's α and β parameters, as well as the break energy, to be calculated reliably.

2.9. 7 mm Band Imaging with the VLBA

2.9.1. Observations

We have obtained 31 total and polarized intensity images of BL Lacertae from 2011 January to 2013 April at 43 GHz (7 mm) with the VLBA as part of the VLBA-BU-BLAZAR monitoring program.[16] The majority of the VLBA observations occurred at approximately monthly intervals. In addition, we obtained three images within two weeks during more intensive campaigns in 2011 September and 2012 April, while in 2012

[16] www.bu.edu/blazars/VLBAproject.html

Table 7
Data from Particular Orbits of the *NuSTAR* Observation Starting on 2012 December 11 (MJD 56272)

	Time (UTC)		Exp.[a]	Photon	Flux in Selected Bands[b]			
Orbit	Start	Stop	(ks)	Index Γ	3–7 keV	7–15 keV	15–31 keV	31–63 keV
1	14:36:20	15:12:30	2.0	1.83 ± 0.04	1.20 ± 0.05	1.23 ± 0.04	1.32 ± 0.08	1.5 ± 0.1
2	15:50:29	16:48:06	2.5	1.81 ± 0.04	1.30 ± 0.05	1.35 ± 0.04	1.47 ± 0.08	1.6 ± 0.1
3	17:27:32	18:25:06	2.4	1.84 ± 0.03	1.26 ± 0.04	1.28 ± 0.04	1.37 ± 0.07	1.5 ± 0.1
4	19:04:29	20:02:07	2.5	1.93 ± 0.04	1.22 ± 0.04	1.18 ± 0.04	1.20 ± 0.07	1.2 ± 0.1
5	20:41:30	21:39:08	2.8	1.90 ± 0.03	1.22 ± 0.04	1.21 ± 0.04	1.26 ± 0.06	1.3 ± 0.1
6	22:18:34	23:16:08	3.2	1.83 ± 0.03	1.06 ± 0.03	1.11 ± 0.03	1.22 ± 0.06	1.4 ± 0.1
7	23:55:28	00:53:09	3.5	1.83 ± 0.03	1.09 ± 0.03	1.14 ± 0.03	1.25 ± 0.06	1.4 ± 0.1
8	01:32:33	02:29:24	3.2	1.93 ± 0.03	1.08 ± 0.03	1.04 ± 0.03	1.06 ± 0.05	1.10 ± 0.08
All	14:36:20	02:29:24	22.1	1.87 ± 0.02	1.15 ± 0.02	1.16 ± 0.02	1.22 ± 0.02	1.29 ± 0.03

Notes. The photon indices Γ and fluxes are from fits of the power-law model to the full band data in each orbit. All uncertainties are 1σ.
[a] Total exposure, deadtime-corrected sum of good-time intervals.
[b] De-absorbed; in units of 10^{-11} erg cm^{-2} s^{-1}. Derived from XSPEC fits to full-band spectra of each orbit.

Table 8
Spectral Model Parameters Fit to *NuSTAR* and Simultaneous *Swift*/XRT Data

Dataset	*NuSTAR*[a]	*NuSTAR* + *Swift*[a,b]
Energy Range	3–70 keV	0.5–70 keV
Power Law Model, `phabs(pow)`		
χ^2/dof	287/283	385/375
Γ (photon index)	1.88 ± 0.01	1.89 ± 0.01
Broken Power Law Model, `phabs(bknpow)`		
χ^2/dof	286/282	377/373
Γ_1 (below E_b)	1.91 ± 0.04	$3.3^{+1.3}_{-0.7}$
E_b (keV)	7 (fixed)	1.0 ± 0.2
Γ_2 (above E_b)	1.86 ± 0.02	1.88 ± 0.01
Log-parabolic Model, `phabs(logpar)`		
χ^2/dof	286/282	381/374
α_{Xlp} (Γ at 7 keV)	1.89 ± 0.02	1.90 ± 0.01
β_{Xlp} (curvature)	−0.03 ± 0.05	−0.04 ± 0.03

Notes. A fixed hydrogen column density of 3.4×10^{21} cm^{-2} is assumed in all models. All uncertainties are 1σ.
[a] The best-fit cross-normalization between FPMA and FPMB is typically 0.99 ± 0.01.
[b] The best-fit cross-normalizations between FPMA and XRT are typically 1.05 ± 0.05 and 0.89 ± 0.06 for observation segments 050 and 053, respectively.

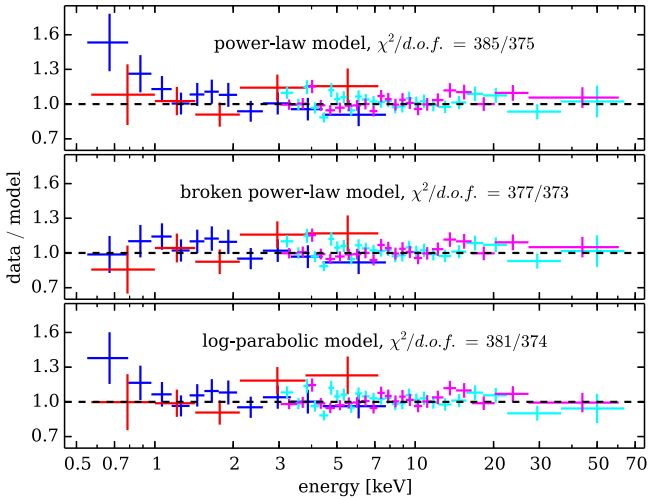

Figure 12. Data-to-model ratios for fits to the contemporaneous *Swift*/XRT and *NuSTAR* data using three simple models. The *NuSTAR* FPMA and FPMB data are shown in cyan and magenta, respectively. The *Swift*/XRT data for Segments 050 and 053 are are shown in blue and red, respectively. The model parameters are given in Table 8.

October we obtained four images within two weeks. We processed and imaged the VLBA data in a manner identical to that described in Jorstad et al. (2005). We performed calibration of the electric vector position angle (EVPA) of polarization using (1) observations with the Jansky Very Large Array (JVLA), carried out close to the epochs of VLBA observations of selected sources from the VLBA-BU-BLAZAR sample, (2) the *D-term* method (Gómez et al. 2002), and (3) the stability of the EVPAs of selected stationary features in sources observed along with BL Lacertae. The accuracy of the EVPA calibration is within 5°–10°. The JVLA observations also provided a check on the amplitude calibration, indicating that the flux estimates have an accuracy of 5%–10%. The analyzed time interval covers both the relatively quiescent period at millimeter wavelengths near the beginning of 2011, the major outburst near the end of 2012, and the first few months of 2013.

2.9.2. Parsec-scale Structure

We model the images in terms of a small number of components with circular Gaussian brightness distributions in the same manner as described in Jorstad et al. (2005). Figure 17 presents a typical VLBA image of BL Lacertae at 43 GHz, with the positions of components marked according to the modeling. At BL Lac's redshift of $z = 0.069$, 1.0 mas corresponds to 1.32 pc, and with an orientation to our line of sight of ∼6° (Jorstad et al. (2005), Marscher et al. (2008), Hovatta et al. (2009), Cohen et al. (2014), 1 mas translates to a deprojected size of ∼13 pc.

The innermost region of the jet in BL Lac consists of three essentially stationary features (see, e.g., Figure 17). We refer to the northernmost of these features, *A*0, as the "core" of the jet at 43 GHz, although *A*0 lies ∼1 pc from the black hole and at least one moving knot has been detected to the north of it (Marscher et al. 2008). Knots *A*1 and *A*2 are located at distances 0.14 ± 0.04 mas (∼1.8 pc deprojected distance) and 0.30 ± 0.03 mas (∼3.9 pc) from the core, respectively, and are classified as

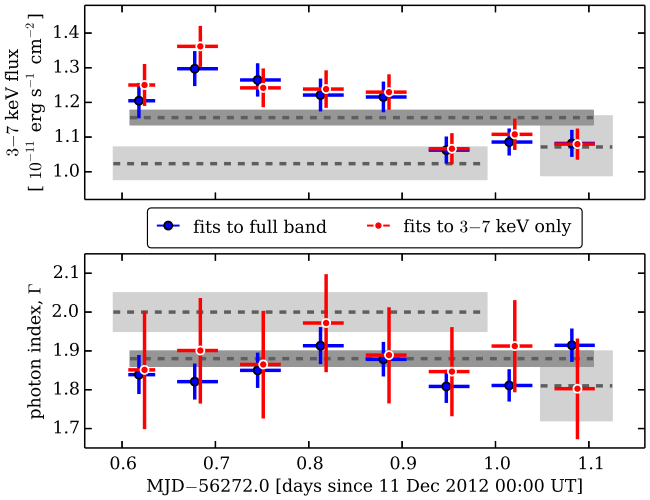

Figure 13. The 3–7 keV flux and photon index for each orbit of the *NuSTAR* observation, derived from power law model fits to the full *NuSTAR* band (blue symbols) and only 3–7 keV band (red symbols). The error bars denote 1σ uncertainties. Light-gray shaded regions mark 1σ confidence regions for fluxes and photon indices for the contemporaneous *Swift* observations, from fits to the full *Swift*/XRT band. The dark-gray shaded regions show the flux and photon index confidence regions for the entire *NuSTAR* observation, fit to the 3–7 keV band only. Dashed horizontal lines denote best-fit values in all cases.

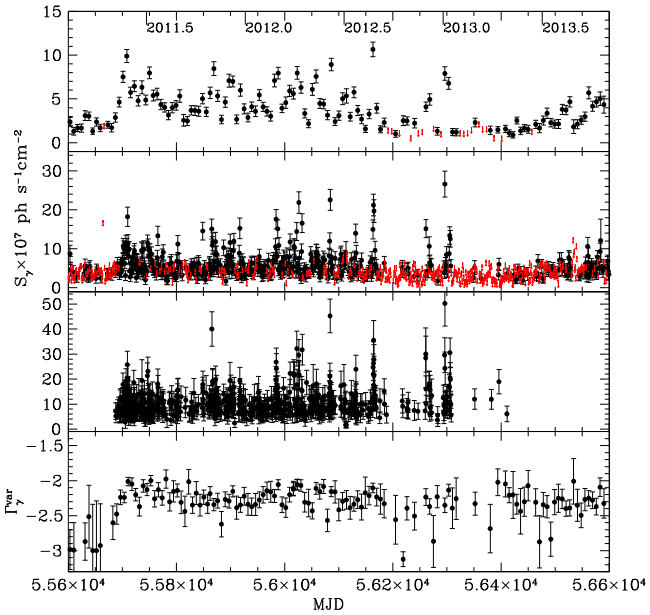

Figure 14. γ-ray light curves of BL Lac from 2011 February 8 to 2013 October 31 in the 0.1–200 GeV band, from the top: (1) with a weekly bin size using a simple power law model with the variable photon index (light curve 4); (2) with a bin size of one day and the spectral model fixed to that given in the 2FGL catalog (light curve 2); (3) with a bin size of 6 hrs and the fixed spectral model (light curve 3; detections only). *Bottom:* dependence of the γ-ray photon index on time for light curve 4.

downstream quasi-stationary features. In a quiescent state, the core contributes ∼50% of the total 43 GHz flux, while the extended jet beyond 0.5 mas from the core carries only ∼10%–15% of that amount, and stationary features *A*1 and *A*2 contribute the rest. In active states, moving knots can be of similar brightness as *A*0 when they start to separate from the core (Figure 18 (*left*); see the discussion of kinematics below).

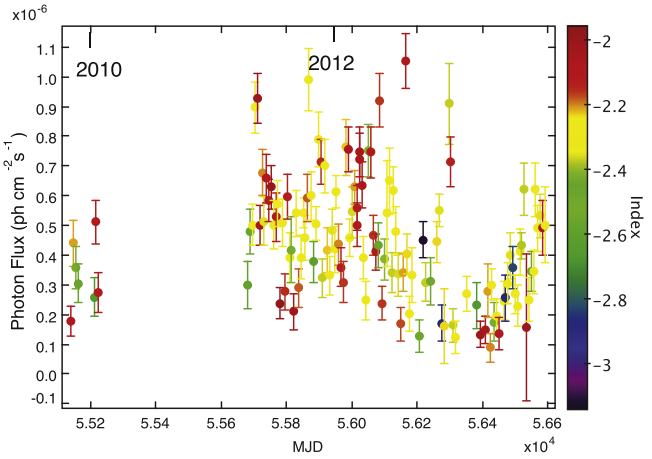

Figure 15. Photon flux (left vertical axis) and photon index (color-coded from 2 (red) to 3 (dark blue) as indicated on right axis) in the 0.1–200 GeV γ-ray band as a function of time in 2009–2013.

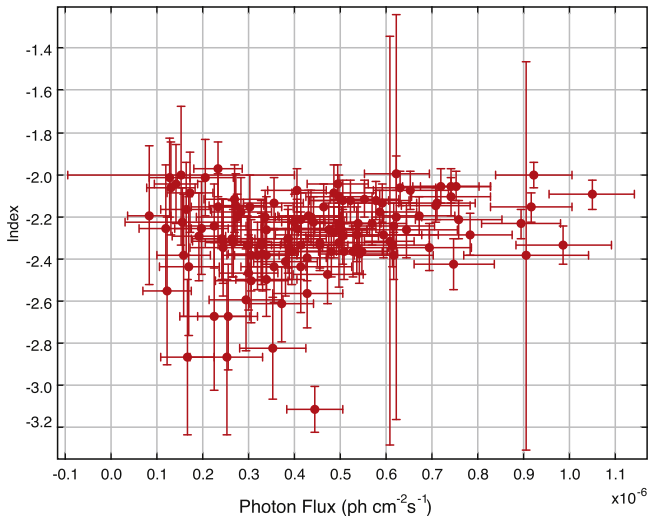

Figure 16. Photon index in the 0.1–200 GeV γ-ray band as a function of photon flux in 2008–2013.

Note that the positions of *A*1 and *A*2 agree, to within the errors, with those of stationary components reported by Stirling et al. (2003), Jorstad et al. (2005), and Marscher et al. (2008). Knot *A*2 is probably the same as knot "ID 7" in the 15 GHz VLBA imaging of Lister et al. (2013).

Another interesting feature apparent in Figure 17 is a region of low brightness ∼1 mas from the core. Bach et al. (2009) explain this feature as the result of reduced Doppler boosting between 0.7 and 1 mas owing to either greater misalignment between the jet direction and our line of sight or a lower Lorentz factor in this region. Knots *C*1-*C*4 are moving features with apparent speeds of 7–10 *c*, similar to those found by Jorstad et al. (2005) and Lister et al. (2009). For another component, "M1," ejected in 1999, $\beta_{\rm app} \sim$ 12–19 *c* was reported by Bach et al. (2009).

3. KINEMATICS OF THE PARSEC-SCALE RADIO JET AND RELATIONSHIP TO FLARING AT OTHER WAVEBANDS

Figure 18 (*right*) presents the light curve of the mm-wave core, *A*0, which reveals an increase of the core brightness

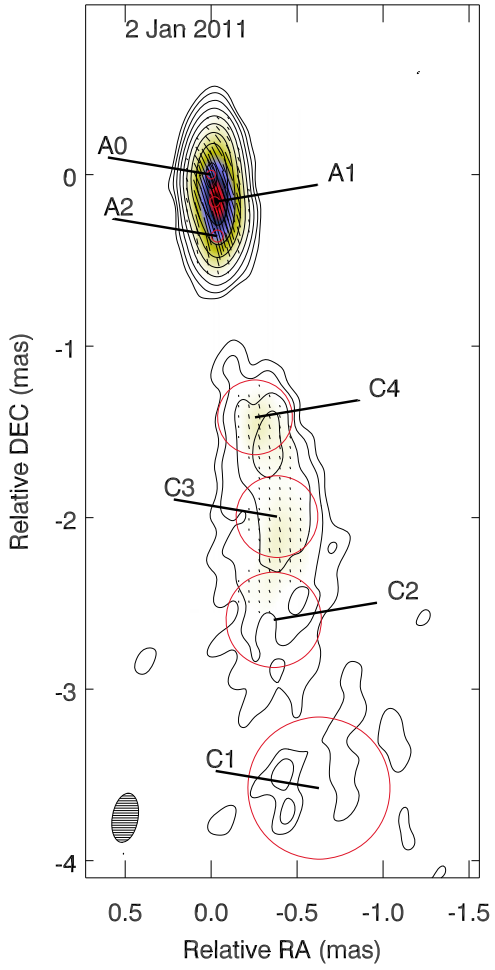

Figure 17. Total (contours) and polarized (color) intensity image of BL Lacertae on 2011 January 2 (MJD 55563.5, several months before the mm-wave outburst began in mid-2011). The peak total intensity is 1.62 Jy beam^{-1}, the peak polarized intensity is 183 mJy beam^{-1}, and the beam size is 0.29 × 0.15 mas at PA = −10°. Black line segments within the image indicate direction of the polarization (electric vector). Red circles indicate position and size of components obtained by modeling with circular Gaussian components. The feature labelled *A*0 is the 43 GHz core.

contemporaneous with the dramatic outburst seen at 1.3 mm and sub-mm wavelengths in 2012 October. Here we analyze the jet kinematics during the peak of this mm-wave outburst.

Figures 19–21 present the total and polarized intensity images of the innermost region of the jet from 2011 March to 2013 April, convolved with a beam corresponding to the resolution of the longest baselines of the VLBA at 43 GHz, ∼0.1 mas. We detect four moving knots during the period from 2011 January to 2013 April. Figure 22 plots the separations of the knots from the core, while Table 9 gives their kinematic parameters. Knots *K*11*a* and *K*11*b*, ejected in 2011, moved significantly more slowly than *K*12*a* and *K*12*b*, which appeared in the jet in 2012.

Using the method proposed by Jorstad et al. (2005) we estimate Doppler, δ, and Lorentz, Γ, factors and the angle between the velocity vector and the line of sight, $\Theta_{\circ}$, of the knots (see Table 9) from the angular sizes and variability timescales of the knots. According to the derived parameters, knot *K*11*b* was ejected along the boundary of the jet closest to the line of sight, if the opening semi-angle of the jet is ∼2°, as found by Jorstad et al. (2005). (Note that *K*11*b* is "knot K11" discussed in Arlen et al. (2013) in connection with the TeV flare of BL Lac observed in 2011 June with VERITAS.) Alternatively, the slower knots could correspond to slow magneto-acoustic waves and the higher-speed knots to fast magneto-acoustic waves (Cohen et al. 2014). Four images are closely spaced in time during October 2012 (Figure 20). Comparison of the polarization vectors and brightness of *A*0 on the 2012 October 20 and 28 (MJD 56220 and 56228) images show that the new knot *K*12*b* probably began to emerge from the core during this week, although the uncertainty of $T_{\circ}$ is significant (Table 9) based on kinematics only.

Knots *K*12*a*, *b* moved three to four times faster than knots *K*11*a*, *b* (see Table 9). The ejection of *K*11*b* may have been followed by an increase in the velocity of the jet flow, which could be the primary cause of the prolonged, 500-day period of intense activity seen in the light curves at millimeter wavelengths and γ-ray energies (Figures 1 and 5; cf. Figure 2 in Raiteri et al. 2013). Using the proper motion of the knots, we estimate the timing of passage of the knots through the stationary features *A*1 and *A*2. Figure 18 (*left*) reveals that the derived epochs of interaction of *K*11*b* and *K*12*b* with *A*2 coincide with 1.3 mm flares observed between MJD ranges 55860–55900 and 56230–56260, respectively. Figure 18 (*right*) shows that after the ejection of each superluminal knot and its passage through *A*1 and *A*2, the flux of the feature (*A*1 or *A*2) steadily increased. This suggests that emission in a quasi-stationary feature is enhanced by such a passage. In addition, when knot *K*11*b* encountered stationary knot *A*2, it brightened and became more highly polarized (Figure 19, epoch 2011 December 2). Similar scenarios were observed when knot *K*12*b* encountered all three stationary knots *A*0 and *A*1 (Figure 20, epoch 2012 October 28 and 29, respectively, and *A*2 (Figure 21, epoch 2012 December 21). Each episode of multi-day mm-wave flaring activity is contemporaneous with several shorter-timescale γ-ray flares (Figure 23).

The higher polarization when superluminal knots *K*11*b* and *K*12*b* reached stationary knot *A*2 could have been caused by an increase in the strength and order of the magnetic field from compression by a stationary shock corresponding to *A*2. This situation bears a striking resemblance to that in 3C 454.3 when new knot *K*09 encountered stationary knot *C* (Wehrle et al. 2012b; Jorstad et al. 2013). Just as in the case of 3C 454.3, the stationary knot's EVPA is always nearly aligned with the jet direction, a signature of a transversely oriented shock with magnetic field compressed along the shock front (Hughes et al. 1985, 1989). Stationary knots *A*1 and *A*2, as well as the radio core *A*0, could be standing conical shocks (Cawthorne 2006). Interactions of compressed plasma behind a moving shock with stationary shocks can result in enhanced acceleration of relativistic electrons, instigating an outburst from mm-wave to γ-ray frequencies. If the plasma is turbulent, the acceleration of the highest-energy electrons might be sporadic, leading to multiple flares and shorter fluctuations in flux, especially at optical and γ-ray frequencies (Marscher 2014).

4. CORRELATIONS AND TIME DELAYS BETWEEN BANDS

We evaluate the time delays between bands by applying the discrete correlation function (DCF) methodology (Edelson & Krolik 1988), as implemented in the *aitlib* library in IDL. We correlate available data on long (5–9 years), medium

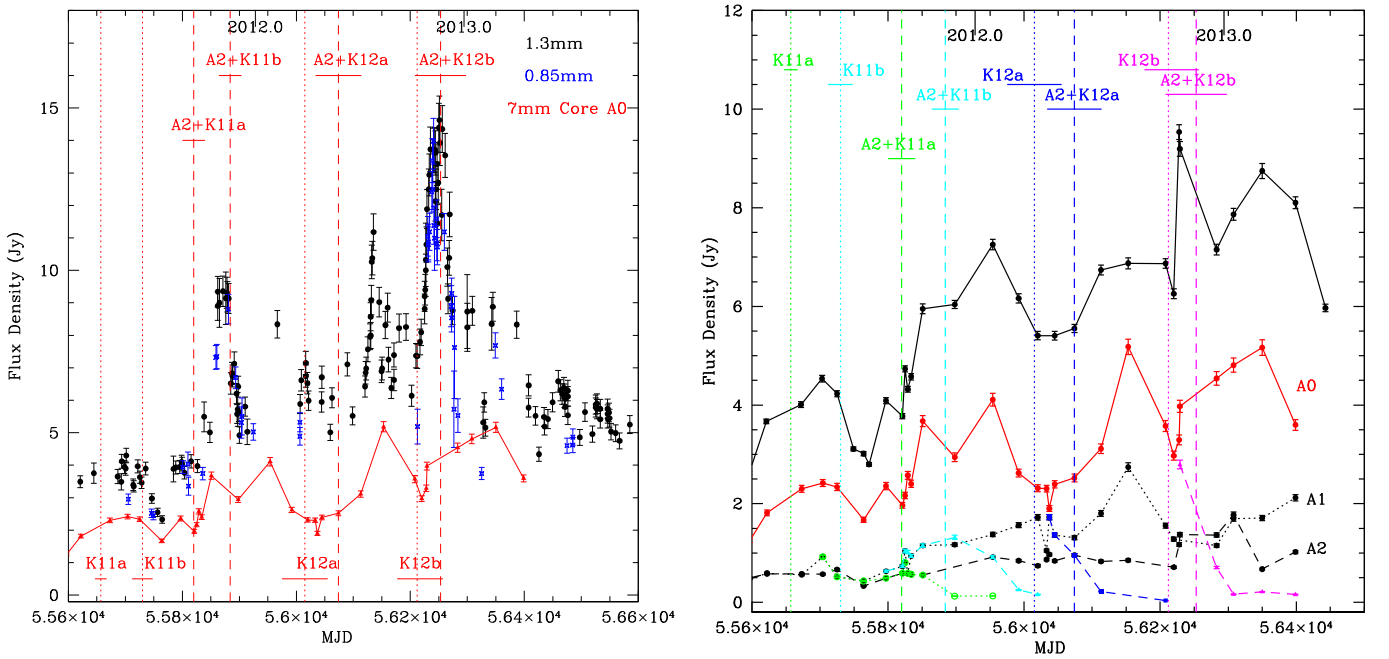

Figure 18. *Left:* light curves at 1.3 mm (black filled circles) and 0.85 mm (blue crosses) from the whole source and at 7 mm from the VLBI core (red triangles); the red dotted lines correspond to the ejection times of the superluminal knots from the core, the red dashed lines mark the epochs of passage of the knots through *A*2. *Right:* light curves of the entire parsec-scale jet (black) at 7 mm, core *A*0 (solid red line), quasi-stationary knots *A*1 (dotted black line) and *A*2 (dashed black line), and moving knots *K*11*a* (green), *K*11*b* (cyan), *K*12*a* (dark blue), *K*12*b* (magenta). Vertical dotted (for ejection times) and dashed lines (epochs of passage) have colors corresponding to the relevant knots. The superluminal knots fade rapidly within two months after ejection from the core and passage through the quasi-stationary knots.

(1–3 years), and short (3 months when the *Herschel* data were obtained) timescales.

4.1. Details of the Data Sampling

Details of the data sampling used for the DCF analysis are as follows:

1. *CARMA 3 mm.* CARMA data at 3 mm over the time range from 2012 August 24 to 2013 October 29, totalling 71 measurements, are used.
2. *SMA 1.3 mm.* SMA data at 1.3 mm over the time range from 2008 January 12 to 2013 October 20, which correspond to 241 measurements, are used for the long-timescale correlation analysis, while 167 measurements from 2011 February 8 to 2013 October 20 are used for the medium-timescale analysis. During the short, three-month active period in 2012 October to 2013 February, we include 28 measurements. During that time period, there are 7 additional days with measurements only in the 0.87 mm band.
3. *Herschel Far-infrared.* We include 14 observations at 250 μm and 19 observations at 160 μm in the 2012 October–2013 February active period.
4. *Fermi LAT.* We use γ-ray light curve 1 starting at the beginning of science operations on 2008 August 5 to 2013 October 31 (273 data points). We replace each non-detection in the γ-ray band with a pseudo-detection at half the upper limit to the flux, with uncertainty equal to this flux. We evaluate variability on a 3 year timescale using γ-ray light curve 2, from 2011 February 8 to 2013 October 31 (371 points). During the three-month active period in 2012 October to 2013 February, there are 26 single-day detections.
5. *Swift XRT and UVOT.* The *Swift* X-ray, optical, and UV light curves cover the 8 year period since the beginning of science operations from 2005 July 26 to 2013 Nov 2 (MJD 53577–56598), with 264, 251, and 249 points at each of the respective bands. During the three-month active period in 2012 October–2013 February, we include 146 X-ray points and 146 UVOT points (there were multiple observations on some days).

4.2. Details of Correlations

To determine the 3σ level of significance of a given correlation, we use the same methodology as in our paper on 3C454.3 (Wehrle et al. 2012b); we have not yet implemented a new, more robust method that has been proposed recently by Emmanopoulos et al. (2013). For each light curve used in the cross-correlation analysis, we generate 5000 simulated light curves binned in the same manner as the observed data and with the same mean and standard deviation of the flux. The simulated light curves follow a power-law power spectral density, $P(\tau) \propto \tau^b$, where τ is the time-scale of the variations with b varied from 1.0 to 2.5 in increments of 0.1. Such a range of b is expected for blazar light curves (e.g., Chatterjee et al. 2012). We compute the DCF between the artificial light curves to determine the 99.7% confidence level for each value of b to estimate the significance of the maxima and minima of the derived DCF of the observed light curves. In our DCF figures, curves representing these 99.7% confidence levels are drawn in gray. For a significant correlation coefficient, we approximate the DCF near the peak by a Gaussian and determine the FWHM, which gives an uncertainty for the given delay.

Figure 24 plots four of the significant long-timescale correlations. We note that we have not found a significant correlation between the γ-ray and V-band light curves;

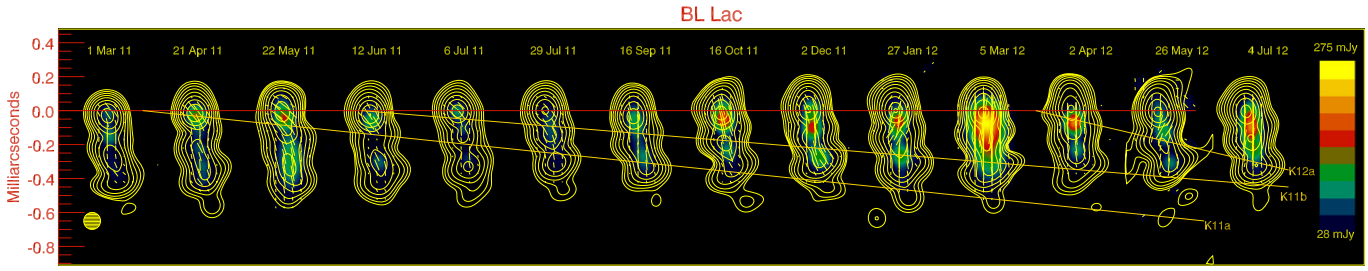

Figure 19. Total (contours) and polarized (color) intensity image of BL Lacertae during the mm-wave outburst, with a peak total intensity of 4.83 Jy beam^{-1}, peak polarized intensity of 338 mJy beam^{-1}, and beam size of 0.1 × 0.1 mas. Yellow line segments within the images indicate direction of the polarization electric vector. Horizontal spacing is sequential, but not directly proportional to the time between observations.

Table 9
Parameters of Superluminal Knots

Parameter	*K*11*a*	*K*11*b*	*K*12*a*	*K*12*b*
μ, (mas yr^{-1})	0.67 ± 0.06	0.58 ± 0.06	1.86 ± 0.16	2.64 ± 0.38
β_{app}	3.0 ± 0.3	2.6 ± 0.3	8.4 ± 0.7	11.9 ± 1.7
T_o, (years)	2011.264	2011.46	2012.24	2012.78
	± 0.025	± 0.05	± 0.11	± 0.12
T_o, (MJD)	55657 ± 10	55730 ± 18	56015 ± 40	56212 ± 45
F_{max}, (Jy)	0.92 ± 0.15	1.32 ± 0.18	1.72 ± 0.20	2.79 ± 0.20
a, (mas)	0.09 ± 0.02	0.09 ± 0.01	0.08 ± 0.01	0.08 ± 0.02
δ	6.1	8.4	9.5	7.3
Γ	3.9	4.7	8.5	13.4
Θ_o, (deg)	7.5	3.9	6.0	7.0

Note. μ—proper motion; β_{app}—apparent speed in units of speed of light c; T_o—time of ejection; F_{max}—maximum flux density; τ_{var}—timescale of flux variability; a—angular size of component at epoch of maximum flux as measured on VLBA images; δ—Doppler factor; Γ—Lorentz factor; Θ_o—angle between velocity vector of component and line of sight.

although there is a maximum of the DCF near 0, it is not statistically significant. Figure 24 shows that (1) the correlation between the γ-ray and 1.3 mm light curves is significant for delays of -143 ± 5 and -87 ± 10 days (independent of the value of b), where a negative delay corresponds to the γ-ray leading the 1.3 mm variations; the delay at -143 days has a higher level of significance. Figure 25 (*left*) presents the DCF between γ-ray light curve 2 with 1-day binning between 2011 February 8 and 2013 October 31, and the 1.3-mm light curve for the same period. The DCF reveals a peak around 50 days with the 1.3-mm light curve leading the γ-ray light curve. Although the peak is marginally significant, this delay corresponds to the average time needed for knots *K*12*a* and *K*12*b* to travel between features *A*0 and *A*2 (see Figure 18 and Table 9) that supports the idea that a mm-wave flare occurs when a superluminal knot passes the core *A*0 while a γ-ray flare originates when the knot passes *A*2. Returning to our discussion of Figure 24, (2) the X-ray/1.3 mm correlation contains a peak at -3 days and a broader but somewhat lower double peak at +2–6 days. This implies that the 1.3 mm variations can either lead or lag the X-ray by 0 to several days; and (3) we also evaluate the time delays between the *Swift* V-band and UVM2 bands, finding that the variations at the two bands are essentially simultaneous (0 ± 0.5 days). Inspection of the 2012–2013 light curves indicates that all six UVOT bands behave in the same way. (4) The X-ray/V-band DCF on timescales of 3 and 12 months indicates that the two bands are correlated on short timescales, but not on longer timescales. The short-term correlation and longer-term non-correlation are apparent by visual inspection of the light curves, where the optical and UV fluxes rise after 2013 March while the X-ray flux declines. On short timescales of three months, the V-band lead the X-ray variations by 0.5 ± 1.0 days. There was no significant correlation between γ-rays and X-rays (DCF not shown). During the 2012 August 24 to 2013 October 29 interval, the 1.3 mm variations led the 3 mm variations by 3 ± 2 days (DCF not shown).

We investigate the delays between the millimeter and far-IR bands on timescales of three months by using the same technique as for 3C454.3 (Wehrle et al. 2012b). We scale the 0.87 mm fluxes by a factor of 1.2 to match the 1.3 mm data, using observations on several days at both bands that took place within a few minutes to derive the scale factor. We also scale the 160 μm fluxes by 1.39 to match the 250 μm data. The resulting light curves are shown in Figure 26. (The same scale factor applied in the far-IR for 3C454.3, which suggests a similar spectral slope of ∼0.42, despite differences in the emitted frequencies and the difference in overall luminosity: 3C454.3 is more distant and much more luminous than BL Lac.) Using the two scaled light curves, we compute the DCFs, as shown in Figure 25 (*right*). There is no significant correlation between the γ-ray and 250 μm variations on the short timescale (medium blue). There is a significant X-ray/250 μm correlation (dark blue) with the far-IR leading the X-ray variations by 1.0 ± 1.0 days (consistent with no delay) with a broad peak. There is a good V-band/250 μm correlation, with 250 μm leading by 0.5 ± 1.0 days (yellow; the delay is essentially zero). There is a significant 250 μm/1.3 mm correlation, with 250 μm leading by 5.5 ± 3.0 days. The number of points used in these DCFs were as follows: γ-ray—101 (of which 26 were bona fide detections), X-ray—94, V-band—93, 250 + 160 μm—25, 1.3 mm—38, 3 mm—71.

4.3. Summary of the Correlations

In summary, on *long* timescales, we find that (1) variations at γ-ray energies (γ-ray light curve 1 in 2008 August 5–2013 October 31) are very well correlated with those at 1.3 mm, with the latter delayed by 143 ± 5 days and a secondary, but statistically significant, DCF peak at 87 ± 10 days delay (we note that Fuhrmann et al. (2014) find a delay at 3 mm of 93 ± 16 days) ; (2) X-ray and 1.3 mm variations are correlated with a delay less than several days, but alternating which band varies first; and (3) variations at the UVM2 and optical V bands were simultaneous to within 0 ± 0.5 days. On *medium* timescales of 1–2 years, the optical and UV bands are correlated, with no delay, and variations at other bands are uncorrelated. However, the DCF between γ-ray light curve 2

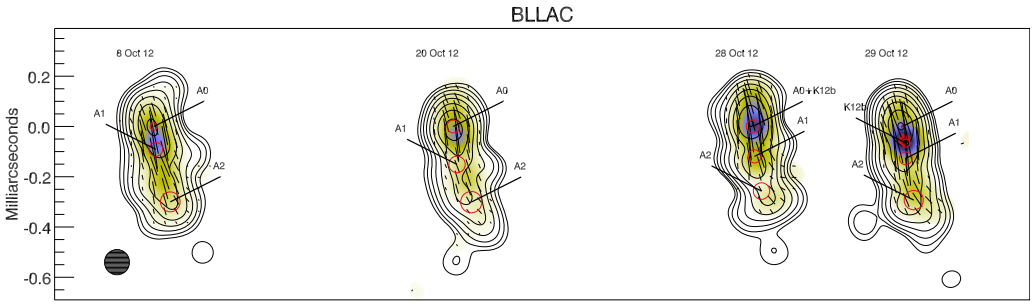

Figure 20. Four closely spaced VLBA images in 2012 October, showing the birth of knot *K12b*. Total (contours) and polarized (color) intensity images (MJDs 56208, 56220, 56228, 56229) with a peak total intensity of 4.05 Jy beam^{-1}, peak polarized intensity of 454 mJy beam^{-1}, and beam size of 0.1 × 0.1 mas. The contour levels are 0.4, 0.8, …51.6, 96% of the peak total intensity. Red circles indicate positions and sizes of components obtained by modeling with circular Gaussian components. Black line segments within the image indicate the direction of the polarization electric vector. The feature labelled *A*0 is the 43 GHz core.

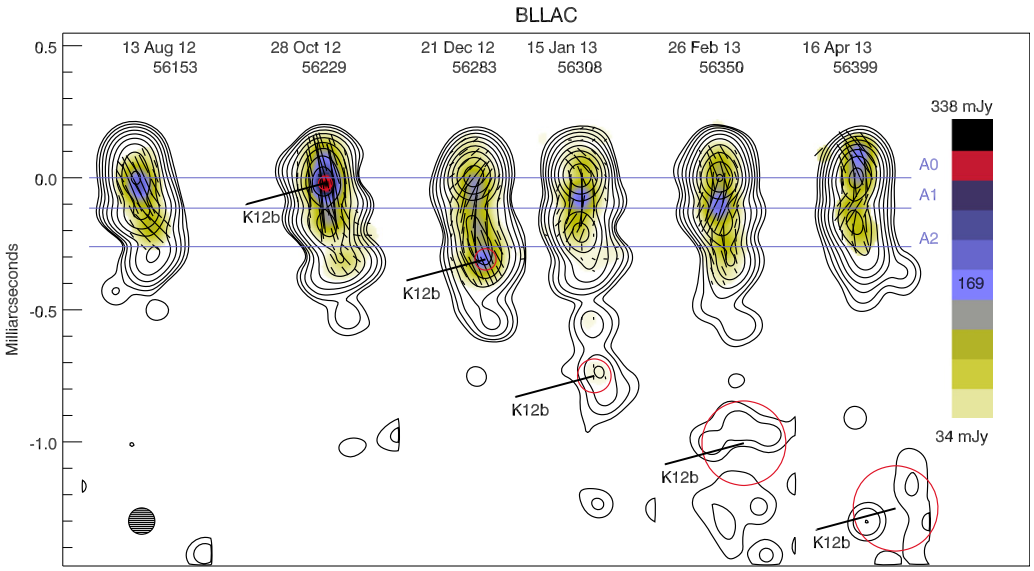

Figure 21. VLBA images obtained in 2012–2013, showing the motion of fast superluminal knot K12b. Total (contours) and polarized (color) intensity images (MJDs 56153, 56228, 56283, 56350, 56399) with a peak total intensity of 4.83 Jy beam^{-1}, peak polarized intensity of 338 mJy beam^{-1}, and beam size of 0.1 × 0.1 mas. The contour levels are 0.4, 0.8, …51.6, 96% of the peak total intensity. Red circles indicate positions and sizes of components obtained by modeling with circular Gaussian components. Black line segments within the image indicate direction of the polarization electric vector. The feature labelled *A*0 is the 43 GHz core.

(2011 February 8–2013 October 31, MJD 55600–56596) and the 1.3 mm light curve during the same period corresponds to a moderately significant correlation, with 1.3 mm variations leading those of γ-rays by 55 $\pm$ 2 days. On *short* timescales of three months when the source was very active in 2012 October–2013 February, we find that the X-ray, optical, and UV variations are correlated; specifically, the optical and UV bands lead the X-ray band by 0.5 $\pm$ 1 days. The γ-ray—250 μm correlation is not significant. The X-ray to 250 μm correlation is significant, with variations at 250 μm preceding those in the X-ray band by 1.0 $\pm$ 1.0 days with a broad peak. There is a strong correlation between V-band and 250 μm variation, with 250 μm leading by 0.5 $\pm$ 1.0 days. Variations at 250 μm are significantly correlated with those at 1.3 mm, with 250 μm leading by 5.5 $\pm$ 3.0 days, which is consistent with higher opacity at longer wavelengths in this region of the spectrum.

5. SPECTRAL ENERGY DISTRIBUTIONS

Our data can be used to form 95 daily SEDs from 2012 October 29 through 2013 January 31. We select SEDs on six dates (MJDs 56229, 56246, 56250, 56267, 56272, and 56304) to illustrate the range of spectral shapes during high, intermediate, and low flux states (Figure 27). One of these dates (MJD 56272) includes intensive monitoring with both *Swift* and *NuSTAR*. During this 95-day period, *Fermi* detected BL Lac on 26 days with 24 hr integrations. Seven of the days on which *Fermi* detected BL Lac include simultaneous *Herschel* observations and, on several more days, *Herschel* observations occurred within one day before or after the *Fermi* 24 hr-integration detections. We find that multiple measurements of fluxes with *Herschel* within 24 hr intervals differ by <19%, typically much less (see Table 1). Hence, we include *Herschel* data in a given SED if they were obtained within $\pm$24 hr of the *Fermi* integration limits. The 0.1–200 GeV γ-ray spectral shape is assumed to follow a log-parabolic form, as for γ-ray light curves 1–3 (see above). Because this is an assumption rather than a direct measurement on a given date, the relative γ-ray fluxes displayed in the figure may be different by a small factor at the lowest three frequencies and possibly by a rather large factor at the highest frequency, where the photon counts are low. The error bars shown correspond solely to the uncertainties in the normalization, since we cannot measure the γ-ray spectrum accurately at enough epochs to determine the level of variations in the spectral shape.

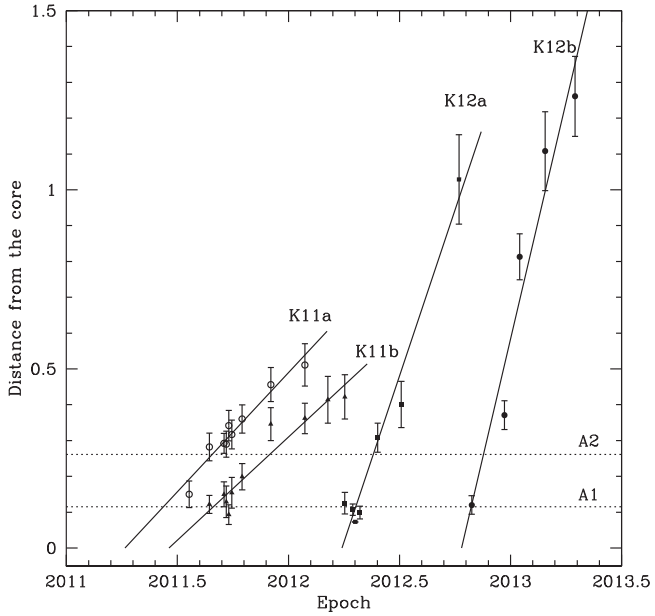

Figure 22. Trajectories and ejection dates of new components *K*11*a*, *K*11*b*, *K*12*a*, and *K*12*b* are shown. The apparent motions of *K*12*a* and *K*12*b* are three to four times higher than for *K*11*a* and *K*11*b*. The locations of quasi-stationary knots *A*1 and *A*2 are also shown.

Inspection of the SEDs in Figure 27 reveals that the high-energy luminosity remains within a factor of 2 of the IR synchrotron luminosity over the entire range of the observations presented here, under the assumption that the actual γ-ray flux when undetected is $\gtrsim$0.5 times the upper limit.

The spectral slopes from millimeter to X-ray wavelengths are very well measured at two epochs. On MJD 56246 (intermediate flux state), $\alpha_{\rm mm-submm} = 0.67 \pm 0.03$, $\alpha_{\rm opt} = 1.71 \pm 0.03$ (where the subscript "opt" refers to near-IR to UV wavelengths), and $\alpha_{\rm X} = 0.77 \pm 0.11$, while on MJD 56267 (high flux state), $\alpha_{\rm mm-submm} = 0.47 \pm 0.03$, $\alpha_{\rm opt} = 1.65 \pm 0.03$, and $\alpha_{\rm X} = 0.74 \pm 0.14$. Although our frequency coverage does not include the high- or low-frequency SED peaks, we can constrain them to lie between 10^{13} and 10^{14} Hz and from 10^{20} to 10^{23} Hz. Intersection of the straight lines that best fit the submillimeter and optical fluxes cross at $10^{13.7}$ Hz ($\sim$60 μm) at both epochs, as is the case for the other epochs to within the accuracy of the spectral index determinations. As discussed previously, the X-ray energy index exhibits a higher level of variability, which can be attributed to changing relative strengths of a steep-spectrum synchrotron component and flatter-spectrum IC emission.

Comparison of BL Lac to 3C454.3, PKS 1510–089 and 3C279. All four objects show a flattening of the SED at wavelengths between 500 and 70 microns (this paper and Hayashida et al. 2012; Nalewajko et al. 2012; Wehrle et al. 2012b). The flattening indicates the presence of a persistent component (presumably the core) and other more evanescent components, some of which may be identified on mm band VLBA images, and all of which are variable.

6. TURBULENT MODEL FOR NONTHERMAL EMISSION FROM BL LACERTAE

The multi-waveband light curves of BL Lacertae exhibit the erratic variability for which the object is renowned. While the major outbursts and changes in polarization on long and medium timescales (e.g., Arlen et al. 2013; Raiteri et al. 2013; Gaur et al. 2014) could conceivably be caused by changes in the direction of the velocity vector of the emitting plasma, as proposed by Raiteri et al. (2013), high-amplitude, seemingly random fluctuations on shorter timescales of days are common. This is an indication that stochastic processes such as turbulence are probably involved, perhaps superposed on more systematic physical processes that affect the emission on longer timescales.

Marscher (2014) argues that turbulent plasma crossing standing shock waves could be responsible for much of the variable nonthermal emission observed in blazars. He is developing the Turbulent Extreme Multi-Zone (TEMZ) model with the goal of reproducing multi-waveband light curves, SEDs, polarization versus time, and both total and polarized images of the cores and other stationary emission features in the jets of blazars. In the numerical TEMZ code, a stationary emission feature is represented by a standing conical "recollimation" shock that is truncated at the downstream end (narrow end of the shock) by a MD, which is a small, thin, strong shock whose front is oriented transverse to the jet axis (often called a "working surface" when it is situated near the end of a jet). The plasma that crosses the MD slows to a speed $\leqslant c/3$ at the MD, and therefore its high-luminosity emission is not strongly beamed in our frame. However, this emission is highly Doppler boosted in the frame of the plasma upstream of the MD, since that plasma is only slightly decelerated by the conical shock, which subtends an angle of $\sim$4°–10° to the jet axis. The MD therefore provides a strong field of synchrotron and synchrotron self Compton seed photons for IC scattering. Seed photons from cells other than the MD are not included yet owing to constraints on run time and memory usage. This is adequate for the most luminous quasars, in which the ratio of high-energy to synchrotron luminosity is $10^{2\pm1}$, but perhaps not for BL Lac objects in which the ratio is of order unity.

The version of the TEMZ code employed in this study divides the jet into 169 cylindrical "computational" cells in a cross-section, with up to 400 cells in each column of cells parallel to the axis, with the the cells starting at the conical shock and ending at a conical rarefaction on the downstream end. The plasma is divided into "turbulent" cells of the same size as the computational cells. One turbulent cell crosses one computational cell during each time step. Further details and a sketch are presented by Marscher (2014).

In the updated version of the TEMZ model discussed here, the plasma upstream of the shock contains a combination of an ordered helical magnetic field and a turbulent field. The latter is given a Kolmogorov spectrum, so that the magnitude of the spatially fluctuating component increases with scale size ℓ as $\Delta B(\ell) \propto \ell^{1/3}$. In order to incorporate this into the computations, the code groups the cells into zones with dimensions of a single cell (ℓ = cell radius), 2 × 2 × 2 cells (ℓ = 2 times the cell radius), 4 × 4 × 4 cells, and 8 × 8 × 8 cells. A new magnetic field component is selected at the upstream edge of each zone, with direction selected randomly and magnitude selected randomly from a log-normal distribution with a standard deviation that is specified by the user (50% is selected here, similar to that found empirically for the solar wind, e.g., Petrosyan et al. 2010). The magnetic field component of each zone is uniformly rotated from one zone boundary to the next, with the sense of the rotation randomly chosen. The magnetic field of each cell is then the weighted vector sum of the

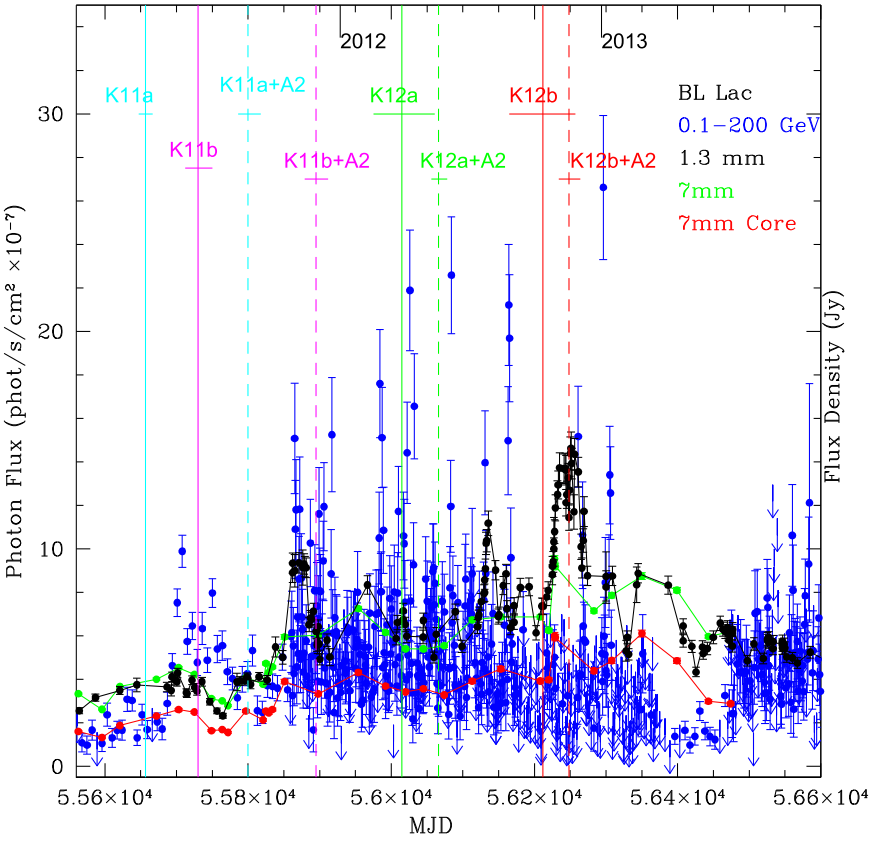

Figure 23. Light curves of BL Lac at γ-ray (blue), 1.3 mm (225 GHz; black) and 7 mm (43 GHz, green) wavelengths, and of the 7 mm core *AO* (red). Ejection dates of new components and dates of their passage through the quasi-stationary knots are indicated by vertical bars.

turbulent components of all four zones containing the cell plus the uniform component. The density of relativistic electrons $n_{\rm re}$ also fluctuates randomly from one zone to the next, following the Kolmogorov scaling of $\Delta n_{\rm re}(\ell) \propto \ell^{2/3}$. The "uniform" component of $n_{\rm re}$ across the jet is varied with proper time in a random fashion with a power spectrum of specified slope that could correspond to a changing injection rate of particles at the base of the jet. The adopted value of this slope is -1.7; see Marscher (2014) for an explanation and details.

A power-law energy distribution of relativistic electrons is assumed to be present as the plasma crosses the standing shock, beyond which the electrons lose energy to synchrotron and IC radiation (off the MD photons). The factor by which a particle's energy increases in a relativistic oblique shock is restricted by the limited number of times that it can reverse direction and re-cross the shock front before being advected downstream. The TEMZ model adopts the following approximate treatment of this. Second-order Fermi acceleration (e.g., Stawarz & Petrosian 2008; Petrosian 2012) or magnetic reconnections (e.g., Sironi & Spitkovsky 2014) in the upstream turbulent plasma could generate a power-law electron energy distribution, with a slope of -2.3 adopted here. Compression at the shock front then increases the particle energies and density. Further energization can occur in those cells where the magnetic field is oriented favorably. The TEMZ code very roughly includes this effect by allowing the maximum energy in rest-mass units, $\gamma_{\rm max}$, of the electrons to increase by a specified factor (left as a free parameter, with a value of 20 in the current BL Lac simulation) if the magnetic field is oriented nearly parallel to the shock normal—the "subluminal" regime within which some particles can cross the shock multiple times before they are swept downstream with the flow (see, e.g., Summerlin & Baring 2012). This creates an extension to the electron energy distribution at the high-energy end in some of the cells. The combination of (1) variations across cells of the magnetic field strength and direction and (2) the small volume filling factor of cells with the highest values of $\gamma_{\rm max}$ shapes the SED produced by the TEMZ model. The result is a progressive steepening of the spectral slope from IR to optical wavelengths, the formation of a UV/soft X-ray tail, broadening the γ-ray SED so that its slope is not exactly that of the optical synchrotron radiation, and occasional flashes of TeV detections. These are all properties possessed by BL Lac.

A run of the TEMZ code with 100% turbulent magnetic field produces the simulated light curves displayed in Figure 28, with a temporal resolution of 5 hr and a total time span of 413 days.[17] The input parameters are adapted to the case of BL Lac, the critical ones (other than those already mentioned) being the upstream systemic bulk Lorentz factor (6), the turbulent (randomly directed) velocity component (chosen to be $c/3^{1/2}$, the ultra-relativistic sound speed), the angle of the conical shock to the jet axis (10°), the viewing angle of the jet (6°), the mean magnetic field upstream of the shock (0.025 G), the ratio of electron to magnetic energy density (0.5), the cell radius (0.004 pc), $\gamma_{\rm max}$ for unfavorable ("superluminal")

[17] Surprisingly, additional runs show that the results change very little if 40% of the mean magnetic field has a steady magnitude with a toroidal configuration. Therefore, the TEMZ model for BL Lac is consistent with observational indications and theoretical arguments for a helical magnetic field on parsec scales (O'Sullivanm & Gabuzda 2009; Cohen et al. 2014).

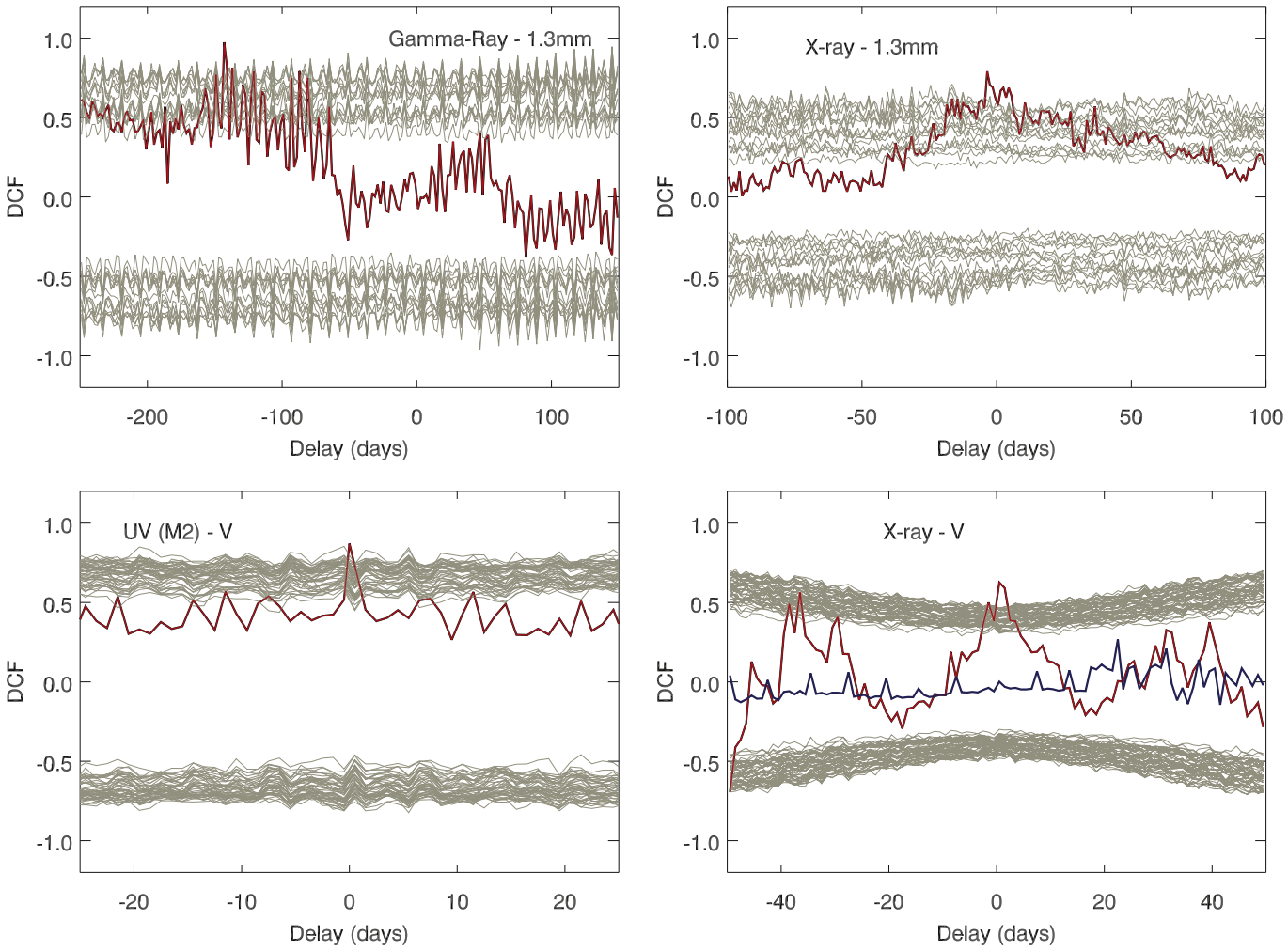

Figure 24. DCF values vs. time lag between observed long-term light curves are shown in red. Correlations that are significant reach the gray bands, which represent chance correlations that occur in only 0.3% of simulated light curves. *Top left:* γ-ray/1.3 mm DCF, whose highest two peaks correspond to a significant correlation, with γ-ray preceding 1.3 mm variations by 143 ± 5 days and 87 ± 3 days on timescales of five years. *Top right:* X-ray/1.3 mm DCF reveals a significant correlation with a broad peak corresponding to alternating positive and negative lags of less than several days on timescales of five years. *Bottom left:* V-band/UVM2 DCF shows significant correlation with no delay (0.0 ± 0.5 days) on timescales of 3 months from 2012 October to 2013 February (red line). *Bottom right:* V-band led X-ray variations by 0.5 ± 1 days, consistent with no lag. On longer timescales of one year from 2012 October to 2013 October, no significant correlation is observed (blue line).

directions of the magnetic field (10^4), the minimum electron energy at the shock front ($\gamma_{\rm min}$, 500), and the jet opening angle (1.9°). The light curves resemble the general features of the observed ones presented in this paper and in Raiteri et al. (2013). SEDs from various time steps are also similar to those observed, as illustrated in Figure 27. The simulated DCF graphs (Figure 29) are partially successful at reproducing features of the observed DCFs. For example, the γ-ray/optical DCF is moderately strong and roughly centered on zero lag. However, some of the observed DCF values do not show significant correlations, while the simulated DCFs always do. There are two likely reasons for this: (1) the TEMZ code produces uniformly sampled fluxes with excellent time coverage, while the sampling of the real long-timescale data is rather sporadic; and (2) the TEMZ model only considers a single standing shock, whereas in BL Lac there are three such stationary emission features, at least at millimeter wavelengths. The observed long-lag γ-ray/1.3 mm correlation is probably the result of γ-ray emission being strongest in component *A*0 (it is not clear if *A*1 and *A*2 emit significant amounts of γ-rays), but 1.3 mm emission being strongest as a moving knot crosses *A*1 and/or *A*2. The degree of success of the TEMZ model will rest on future improvements to make the code more realistic with fewer adustable parameters, and on further development and application of diagnostic comparisons with actual data.

7. SUMMARY OF OBSERVATIONAL AND THEORETICAL MODELING RESULTS

We have presented a rich collection of multi-waveband flux measurements of BL Lacertae over a time span that includes major outbursts that are apparent at all wavebands from millimeter-wave to γ-ray. The inclusion of data from a wide range of orbiting and ground-based telescopes has allowed us to construct SEDs at many epochs while minimizing the frequency gaps. We find that, while the SED maintains its basic double-humped shape, with peaks maintained at roughly constant frequencies, the spectral index within each waveband changes with time.

Superposed on the extended high-flux states of BL Lac is erratic flaring, with the flux changing by more than a factor of

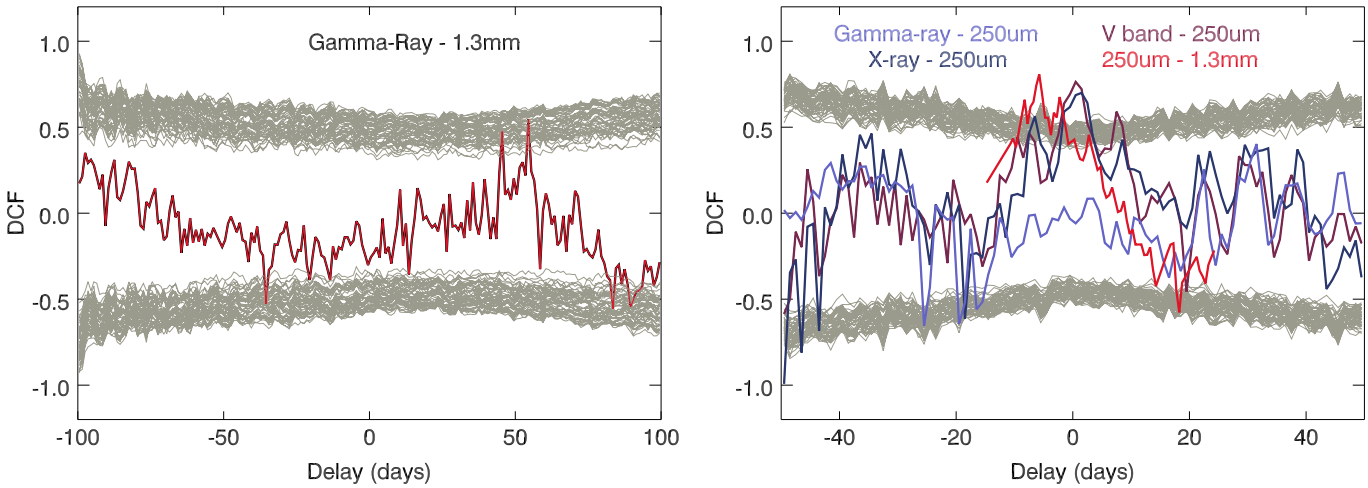

Figure 25. *Left:* DCF between γ-ray light curve 2 and 1.3 mm light curve during the same time range. *Right:* DCFs between *Herschel* 250 μm measured-and-scaled data with other wavebands on timescales of 3 months from 2012 October to 2013 February. Correlations that are significant reach the gray bands, which represent chance correlations that occur in only 0.3% of simulated light curves. γ-ray/250 μm correlation is not significant (medium blue). X-ray to 250 μm DCF (dark blue) indicates that 250 μm precede X-ray variations by 1.0 ± 1.0 days, consistent with zero average lag but with a broad peak. V-band/250 μm shows a good correlation with 250 μm preceding V-band variations by 0.5 ± 1.0 days (yellow). 250 μm/1.3 mm DCF corresponds to a significant correlation, with 250 μm preceding 1.3 mm variations by 5.5 ± 3.0 days.

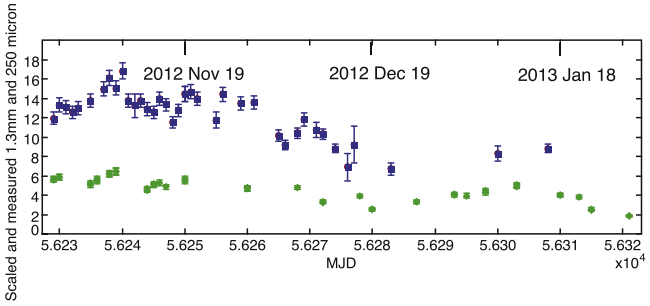

Figure 26. Light curves of measured and scaled data at 1.3 mm (+0.87 mm) band in blue and 250 μm (+160 μm) band in green are shown to illustrate time coverage and variations in flux density. Original data are shown in Figure 4.

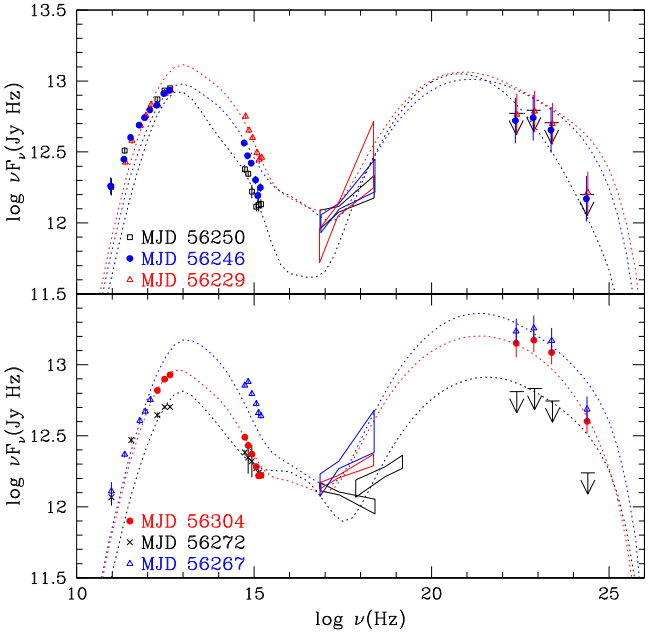

Figure 27. SEDs at six epochs, constructed from data presented in this paper after removal of the effects of reddening, host-galaxy emission, and X-ray absorption. The four flux points from $\log \nu(\mathrm{Hz}) = 22.38$ to 24.68 assume a log-parabolic γ-ray spectral shape, with all parameters fixed except for the flux normalization. Dotted curves correspond to SEDs from different time steps from a simulation with the TEMZ model, selected such that they are similar to the observed SEDs drawn with the same colors.

>2 on a $\lesssim$1 day timescale. These shorter-timescale variations are only sometimes coincident at the various well-separated wavebands. This combination of correspondences and discrepancies, combined with the incomplete time coverage, weakens the correlations of flux variations across wavebands.

As in past studies, the innermost jet structure at millimeter wavelengths as imaged by the VLBA at 43 GHz continues to consist of three bright quasi-stationary knots, *A*0, *A*1, and *A*2. The northern-most (closest to the base of the jet) of these is *A*0, referred to as the "core." All three may represent standing shocks caused by pressure mismatches with the medium surrounding the jet (Marscher et al. 2008) or, for *A*2, the modified fast magnetosonic point (Cohen et al. 2014). In support of this, the polarization at the location of *A*2 increased as two of the moving knots crossed it, consistent with compression of the magnetic field by a shock front. The two bright knots ejected in 2012 had apparent speeds 3–4 times higher than those that appeared in 2011. This can be explained if the knots do not fill the entire cross-section of the jet (see Jorstad et al. 2005; Lister et al. 2013, for general evidence of this) and trajectories of the slower knots lie along the far side of the jet, perhaps augmented by an increase in the flow velocity in 2012. The higher Doppler factor of the emitting plasma in 2012 can explain the $\sim$500 days major outburst that began in 2012 October, as would be the case in the scenario favored by Raiteri et al. (2013), although we note that the flux state and activity in 2011, when the slower knots appeared, were elevated significantly relative to 2010. An alternative explanation of the variations in apparent speed posits that the faster/slower knots are caused by fast/slow magneto-acoustic waves (Cohen et al. 2014). The difference in multi-waveband behavior of fast versus slow waves needs to be explored before the viability of this explanation can be judged.

The passage of knots *K*11*b* and *K*12*b* through quasi-stationary feature *A*2 0.3 mas from the core coincided with

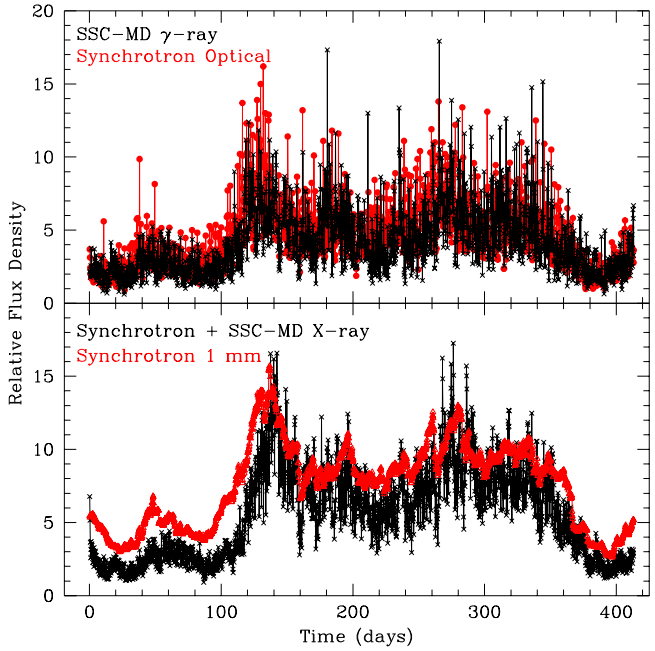

Figure 28. Artificial light curves produced by the TEMZ code with parameters adapted to the case of BL Lacertae (see text).

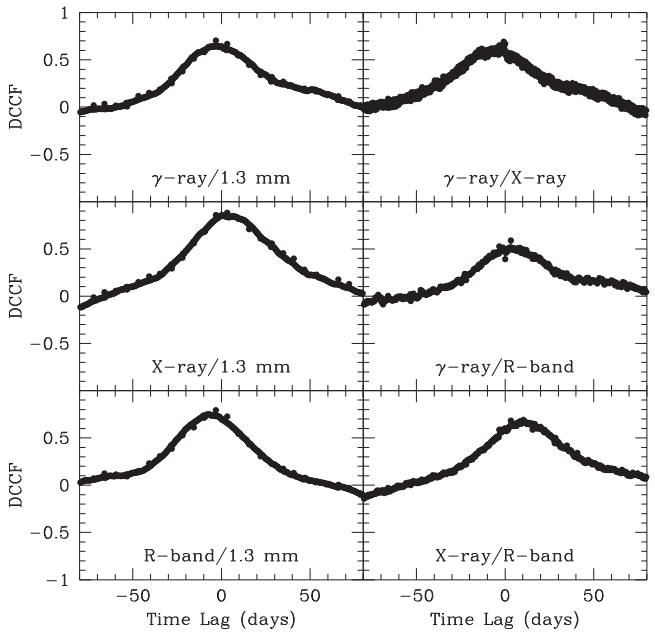

Figure 29. Discrete correlation function curves from the TEMZ simulation for different pairs of wavebands. Negative lag corresponds to variations at the waveband listed first leading those at the second waveband.

flares at $\lambda 1.3$ mm. Furthermore, each episode of multi-day flaring at 1.3 mm coincided with a shorter-term γ-ray flare. Nevertheless, the correlation of the γ-ray and 1.3 mm fluxes is strongest at delays of -143 ± 5 and -87 ± 10 days (γ-ray variations leading), which is similar to the time required for the moving knots to propagate from $A0$ to $A1$ or $A2$. It therefore appears that the strongest γ-ray flares occur when a moving knot interacts with $A0$, while the strongest mm-wave flares occur when such a knot crosses standing shocks $A1$ or $A2$.

The TEMZ model, in which turbulent plasma in the relativistic jet crosses a standing conical shock, reproduces many features of the light curves and SEDs of BL Lac. (It also generates polarization variability similar to the observed behavior, although we do not include a discussion of the polarization here.) Some of the correlations across wavebands are stronger in the simulated than in the actual data. This may be the result of the non-uniformly sampled observations. In addition, the model considers turbulent plasma flowing through only a single stationary emission feature, whereas at least at millimeter wavelengths BL Lac contains three such features.

8. PHYSICAL PICTURE AND CONCLUSIONS

We propose the following physical picture. Within 5 pc of the SMBH, the jet of BL Lac contains three quasi-stationary shock locations—$A0$, $A1$, and $A2$ (see Figure 21)—where most of the millimeter and FIR emission occurs. In response to fluctuating injection of energy into the jet, density enhancements containing high-energy particles appear as superluminally moving blobs. When moving blobs pass through $A0$ or $A2$, the electrons are accelerated to energies up to $\gamma_e \sim 2 \times 10^5$ and we detect IC γ-ray and synchrotron X-ray flares. The event should include IC X-ray and synchrotron millimeter-wave flares, but these can be relatively weak if the low-energy cut-off $\gamma_{\rm min} \gtrsim 1000$ and the magnetic field $B \gtrsim 0.3$ G as the blob crosses the shock, such that 230 GHz falls below the critical frequency of the lowest-energy electrons. Millimeter-wave (synchrotron) flares occur when moving blobs pass through $A1$ as well, but $A1$ seems incapable of accelerating electrons to sufficient energies to produce strong γ-ray IC and optical–X-ray synchrotron flares. This implies that $A0$ and $A2$ may be strong recollimation shocks (as advocated by Cohen et al. 2014, in the case of $A2$), while shock $A1$ is weaker.

In the simplest case of a single injection of energy, this scenario predicts that there should be three flares at millimeter wavelengths and at X-ray energies, with the X-ray spectrum flattening as the IC emission rises. The first and third of these flares should be accompanied by an optical, UV, and X-ray synchrotron flare plus a γ-ray IC flare. When the energy injection into the jet remains elevated for an extended period, multi-flare outbursts occur at all wavebands. Multiple injections of energy result in multiple locations flaring (or near minimum flux) at various times at these wavelengths. Evidence for this can be seen in Figure 18, which demonstrates that the total flux curves at millimeter wavelengths represent a superposition of emission from $A0$, $A1$, and $A2$, with the flux of each varying erratically. The relative timing of the peaks of flares can fluctuate because of the complex emission structure consisting of three standing shocks that are traversed at different times by successive blobs of enhanced density. This causes the relationships between the light curves at the various wavebands to be complex as well, as we observe.

In conclusion, we have found that the strength and nature of the correlations among the flux variations of the different wavebands depend on the time spans of the data. Our results demonstrate how very long data trains including parsec-scale imaging can be used to describe—and compare with theoretical expectations—the wide range of behavior of BL Lac and, ultimately, to derive a physical picture of the structure and energetics of the relativistic jet within five parsecs of its central supermassive black hole.

We thank the anonymous reviewer for comments that improved the paper. We thank Paul Smith (Steward

Table 10
Observed *RXTE* 2.4–10 keV Fluxes and X-Ray Spectral Slopes α_X and Count Rates of BL Lac

JD-245000	Integration Time (s)	$F_{2.4-10\ keV}$[a]	$F_{2.4-10\ keV}$ Error	α_X	α_X Error	Count Rate	Count Rate Error
3433.6507	1856	1.17E-11	4.77E-13	1.06	0.12	1.33	0.05
3436.1616	1248	1.07E-11	5.55E-13	0.71	0.15	1.25	0.06
3438.6360	1968	1.21E-11	4.56E-13	0.70	0.11	1.40	0.05
3440.6464	992	1.46E-11	6.45E-13	0.87	0.13	1.70	0.07
3442.9718	1440	1.42E-11	5.47E-13	0.83	0.11	1.63	0.06
3445.5803	1744	1.30E-11	4.93E-13	0.96	0.11	1.51	0.05
3447.5466	1936	1.18E-11	4.64E-13	0.94	0.11	1.35	0.05
3450.7678	2384	1.40E-11	4.34E-13	0.74	0.09	1.60	0.05
3452.6133	1840	9.92E-12	4.69E-13	0.77	0.14	1.13	0.05
3454.6264	1824	1.38E-11	5.00E-13	0.79	0.11	1.54	0.05

Note.
[a] Observed 2.4–10 keV flux in units of erg s^{-1} cm^{-2}.

(This table is available in its entirety in machine-readable form.)

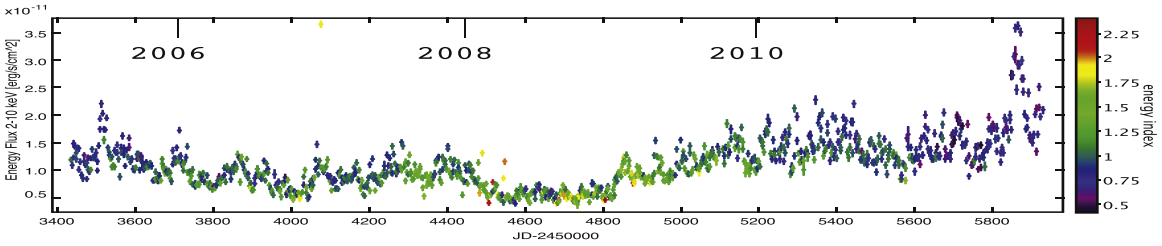

Figure 30. *RXTE* PCA lightcurve from 2005 March 3 to 2011 December 31. The spectral index is color-coded.

Observatory) and Claudia Raiteri (Osservatorio Astrofisico di Torino) for helpful discussions. We are grateful to Göran Pilbratt (Herschel) and Neil Gehrels (*Swift*) for allocation of Target of Opportunity time. We thank Mark Kidger and Rosario Lorente (Herschel Science Centre) for advice in observing with *Herschel*, David Shupe (NASA Herschel Science Center) for assistance with data reduction, and the *Swift* schedulers (*Swift* Operations Center at Pennsylvania State University) for responsive scheduling. A. Wehrle is grateful to Penny Milbouer (Houston, TX) for helpful discussions.

A. Wehrle acknowledges Guest Investigator support from NASA via *Herschel* RSA 1427799. The Boston University group acknowledges support by NASA under *Fermi* Guest Investigator grants NNX11AQ03G, NNX12AO79G, NNX13AP06G, and NNX14AQ58G, and *Swift* Guest Investigator grants NNX14AC59G. S. G. Jorstad acknowledges support from Russian RFBR grant 15-02-00949 and St. Petersburg University research grant 6.38.335.2015. The Submillimeter Array is a joint project between the Smithsonian Astrophysical Observatory and the Academia Sinica Institute of Astronomy and Astrophysics and is funded by the Smithsonian Institution and the Academia Sinica. The VLBA is an instrument of the National Radio Astronomy Observatory. The National Radio Astronomy Observatory is a facility of the National Science Foundation operated under cooperative agreement by Associated Universities, Inc. This research has made use of the XRT Data Analysis Software (XRTDAS) developed under the responsibility of the ASI Science Data Center (ASDC), Italy.

Swift at PSU is supported by NASA contract NAS5-00136.

M. Baloković acknowledges support from the International Fulbright Science and Technology Award and from NASA Headquarters under the NASA Earth and Space Science Fellowship Program, grant NNX14AQ07H.

Part of this work was supported under NASA Contract No. NNG08FD60C, and made use of data from the *NuSTAR* mission, a project led by the California Institute of Technology, managed by the Jet Propulsion Laboratory, and funded by the

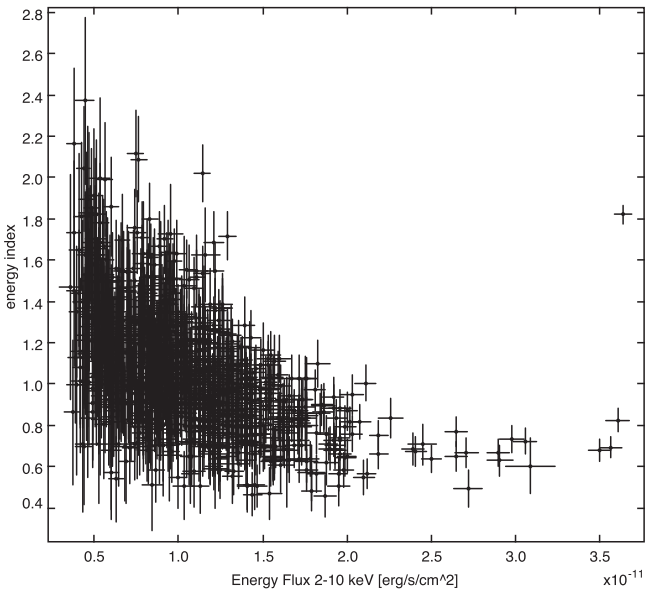

Figure 31. *RXTE* PCA energy index as a function of X-ray brightness. The spectral index tended to flatten when the source was bright, and conversely, steepen when the source was faint. However, X-ray spectra with $\alpha_X \sim 0.5$ occasionally occurred over the full range of observed brightness.

National Aeronautics and Space Administration. We thank the *NuSTAR* Operations, Software and Calibration teams for support with the execution and analysis of these observations. This research has made use of the *NuSTAR* Data Analysis Software (NuSTARDAS) jointly developed by the ASI Science Data Center (ASDC, Italy) and the California Institute of Technology (USA).

T. Hovatta acknowledges support from the Jenny and Antti Wihuri foundation and Academy of Finland project number 267324. Support for CARMA construction was derived from the Gordon and Betty Moore Foundation, the Kenneth T. and Eileen L. Norris Foundation, the James S. McDonnell Foundation, the Associates of the California Institute of Technology, the University of Chicago, the states of California, Illinois, and Maryland, and the National Science Foundation. Ongoing CARMA development and operations are supported by the National Science Foundation under a cooperative agreement, and by the CARMA partner universities.

The Fermi LAT Collaboration acknowledges generous ongoing support from a number of agencies and institutes that have supported both the development and the operation of the LAT as well as scientific data analysis. These include the National Aeronautics and Space Administration and the Department of Energy in the United States, the Commissariat lEnergie Atomique and the Centre National de la Recherche Scientifique/Institut National de Physique Nuclaire et de Physique des Particules in France, the Agenzia Spaziale Italiana and the Istituto Nazionale di Fisica Nucleare in Italy, the Ministry of Education, Culture, Sports, Science and Technology (MEXT), High Energy Accelerator Research Organization (KEK) and Japan Aerospace Exploration Agency (JAXA) in Japan, and the K. A. Wallenberg Foundation, the Swedish Research Council and the Swedish National Space Board in Sweden. Additional support for science analysis during the operations phase is gratefully acknowledged from the Istituto Nazionale di Astrofisica in Italy and the Centre National dtudes Spatiales in France.

This research has made use of the NASA/IPAC Extragalactic Database (NED) which is operated by the Jet Propulsion Laboratory, California Institute of Technology, under contract with the National Aeronautics and Space Administration.

Facilities: Herschel, *Fermi*, *Swift*, SMA, CARMA, *NuSTAR*, VLBA.

APPENDIX
HISTORICAL *RXTE* OBSERVATIONS FROM 2005 THROUGH 2011

The BU group obtained 2.4–10 keV X-ray fluxes with the *RXTE* PCA three times per week from 2005 March 3 to 2011 December 31, after which the instrument was decommissioned. Most of the 1036 observations had integration times between 1400 and 2100 s (see Table 10). We processed the data as described by Marscher et al. (2008), fitting the photon count spectrum with a single power law plus photoelectric absorption corresponding to a neutral hydrogen column density of $2.7 \times 10^{21}\,\mathrm{cm}^{-2}$ (Madejski et al. 1999). We note that Abdo et al. (2011) found that changing the absorbing column density from $N_{\rm H} = 2.0 \times 10^{21}\,\mathrm{cm}^{-2}$ to $3.6 \times 10^{21}\,\mathrm{cm}^{-2}$ changes the energy index by less than 0.02. We estimate that a similar increase from $N_{\rm H} = 2.7 \times 10^{21}\ \mathrm{cm}^{-2}$ to $3.4 \times 10^{21}\,\mathrm{cm}^{-2}$ changes the flux by $\lesssim$5%; since the *RXTE* data are shown primarily for historical context and to demonstrate changes of the energy index with brightness, we have not re-reduced the data with the larger, more current value of the hydrogen column density, $N_{\rm H} = 3.4 \times 10^{21}\ \mathrm{cm}^{-2}$ (Raiteri et al. 2010). The first years of the *RXTE* results were presented separately in Marscher et al. (2008).

During the time period covered here (2005–2011), the energy flux in the 2.4–10 keV band averaged $(1.08 \pm 0.05) \times 10^{-11}\,\mathrm{erg\,s^{-1}\,cm^{-2}}$, corresponding to count rates of $1.10\,\mathrm{cts\,s^{-1}} \pm 0.05\,\mathrm{cts\,s^{-1}}$. The lightcurve is shown in Figure 30. The energy index averaged 1.04 ± 0.163. The energy index tended to be flatter when the source was brighter and steeper when the source was fainter, as shown in Figure 31.

REFERENCES

Abdo, A. A., Ackermann, M., Ajello, M., et al. 2011, ApJ, 730, 101
Agudo, I., Jorstad, S. G., Marscher, A. P., et al. 2011, ApJ, 726, 13
Arlen, T., Aune, T., Beilicke, M., et al. 2013, ApJ, 762, 92
Bach, U., Villata, M., Raiteri, C. M., et al. 2009, A&A, 456, 105
Breeveld, A. A., Curran, P. A., Hoversten, E. A., et al. 2010, MNRAS, 406, 1687
Burrows, D., Hill, J. E., Nousek, J. A., et al. 2005, SSRv, 120, 165
Capetti, A., Raiteri, C. M., & Buttiglione, S. 2010, A&A, 516, 59
Cawthorne, T. V. 2006, MNRAS, 367, 851
Chatterjee, R., Bailyn, C. D., Bonning, E. W., et al. 2012, ApJ, 749, 191
Cohen, M. H., Meier, D. L., Arshakian, T. G., et al. 2014, ApJ, 787, 151
Cutini, S. on behalf of The Fermi LAT Collaboration 2012, ATel, 4028, 1
Edelson, R. A., & Krolik, J. H. 1988, ApJ, 333, 646
Ehgamberdiev, Sh. A., Mirzaqulov, D. O., Buemi, C. S., et al. 2012, ATel, 4271, 1
Emmanopoulos, D., McHardy, I. M., & Papadakis, I. E. 2013, MNRAS, 433, 907
Fuhrmann, L., Larsson, S., Chiang, J., et al. 2014, MNRAS, 449, 1899
Gaur, H., Gupta, A. C., Witta, P. J., et al. 2014, ApJL, 781, L4
Gómez, J. L., Marscher, A. P., Alberdi, A., Jorstad, S., & Agudo, I. 2002, VLBA Scientific Memo 30 (NRAO), (https://science.nrao.edu/facilities/vlba/publications/memos/sci)
Griffin, M. J., Abergel, A., Abreu, A., et al. 2010, A&A, 518, L3
Gurwell, M. A., Peck, A. B., Hostler, S. R., Darrah, M. R., & Katz, C. A. 2007, in ASP Conf. Ser. 375, From Z-Machines to ALMA: (Sub)Millimeter Spectroscopy of Galaxies, ed. A. J. Baker et al. (San Francisco, CA: ASP), 234
Grupe, D., & Wehrle, A. E. 2012, ATel, 4627, 1
Harrison, F. A., Craig, W. W., Christensen, F. E., et al. 2013, ApJ, 770, 103
Hayashida, M., Madejski, G. M., Nalewajko, K., et al. 2012, ApJ, 754, 114
Hill, J. E., Burrows, D. N., Nousek, J. A., et al. 2004, Proc. SPIE, 5165, 217
Hovatta, T., Valtaoja, E., Tornikoski, M., & Lähteenmäki, A. 2009, A&A, 494, 527
Hughes, P. A., Aller, H. D., & Aller, M. F. 1985, ApJ, 298, 301
Hughes, P. A., Aller, H. D., & Aller, M. F. 1989, ApJ, 341, 54
Jorstad, S. G., Marscher, A. P., Smith, P. S., et al. 2013, ApJ, 773, 147
Jorstad, S. G., Marscher, A. P., Lister, M. L., et al. 2005, AJ, 130, 1418
Karamanavis, V., Myserlis, I., Fuhrmann, L., et al. 2012, ATel, 4349, 1
Larionov, V., Blinov, D., & Konstantinova, T. 2012, ATel, 4031, 1
Lister, M. L., Aller, M. F., Aller, H. D., et al. 2013, AJ, 146, 120
Lister, M. L., Cohen, M. H., Homan, D. C., et al. 2009, AJ, 138, 1874
Madejski, G., Sikora, M., Jaffe, T., et al. 1999, ApJ, 521, 145
Malmrose, M. P., Marscher, A. P., Jorstad, S. G., Nikutta, R., & Elitzur, M. 2011, ApJ, 732, 116
Marscher, A. P. 2014, ApJ, 780, 87
Marscher, A. P., Jorstad, S. G., D'Arcangelo, F. D., et al. 2008, Natur, 452, 966
Nalewajko, K., Sikora, M., Madejski, G. M., et al. 2012, ApJ, 760, 69
Nolan, P. L., Abdo, A. A., Ackermann, M., et al. 2012, ApJS, 199, 31
O'Sullivanm, S. P., & Gabuzda, D. C. 2009, MNRAS, 393, 429
Petrosian, V. 2012, SSRv, 173, 535
Petrosyan, A., Balogh, A., Goldstein, M. L., et al. 2010, SSRv, 156, 135
Pilbratt, G. L., Riedinger, J. R., Passvogel, T., et al. 2010, A&A, 518, L1
Plotkin, R. M., Anderson, S. F., Brandt, W. N., et al. 2012, ApJL, 745, L27
Poglitsch, A., Waelkens, C., Geis, N., et al. 2010, A&A, 518, L2
Poole, T. S., Breeveld, A. A., Page, M. J., et al. 2008, MNRAS, 383, 627
Raiteri, C. M., Villata, M., D'Ammando, F., et al. 2013, MNRAS, 436, 1530
Raiteri, C. M., Villata, M., Bruschini, L., et al. 2010, A&A, 524, 43

Roming, P. W. A., Kennedy, T. E., Mason, K. O., et al. 2005, SSRv, 120, 95
Sault, R. J., Teuben, P. J., & Wright, M. C. H. 1995, in ASP Conf. Ser. 77, In Astronomical Data Analysis Software and Systems IV, ed. R. Shaw, H. E. Payne & J. J. E. Hayes (San Francisco, CA: ASP), 433
Sironi, L., & Spitkovsky, A. 2014, ApJL, 783, L21
Stawarz, L., & Petrosian, V. 2008, ApJ, 681, 1725
Stirling, A. M., Cawthorne, T. V., Stevens, J. A., et al. 2003, MNRAS, 341, 405
Stroh, M. C., & Falcone, A. D. 2013, ApJS, 207, 28
Summerlin, E. J., & Baring, M. G. 2012, ApJ, 745, 63
Tanihata, C., Takahashi, T., Kataoka, J., et al. 2000, ApJ, 543, 124
Taylor, M. 2005, in ASP Conf. Ser. 347, 29 topcat software available via download from http://www.star.bris.ac.uk/~mbt/topcat/
Urry, C. M., & Padovani, P. 1995, PASP, 107, 803
Vermeulen, R. C., Ogle, P. M., Tran, H. D., et al. 1995, ApJ, 452, 5
Wehrle, A. E., Grupe, D., Gurwell, M., Jorstad, S., & Marscher, A. 2012a, ATel, 4557, 1
Wehrle, A. E., Marscher, A. P., Jorstad, S. G., et al. 2012b, ApJ, 758, 72